1 **Regular Article**

2

# 3 *TET2*-mutant clonal hematopoiesis prevents T-cell exhaustion and 4 suppresses cancer metastasis

5

6 Ai Nhan Thi Le[1], Manabu Fujisawa[2,3], Giacomo Campo[4], Yen T M Nguyen[2], Tran B.
7 Nguyen[2], Sakurako Suma[2, 5], Yasuhito Suehara[2, 5], Fumihito Miura[6], Hiromitsu Araki[7],
8 Kenichi Makishima[2, 5], Tatsuhiro Sakamoto[2, 5], Mizuho Nakayama[8, 9], Masanobu Oshima[8, 9],
9 Miwako Kakiuchi[10], Shumpei Ishikawa[10], Chizu Tanikawa[11], Koichi Matsuda[11], Ryunosuke
10 Saiki[12, 13], Seishi Ogawa[12, 13], Vanner, Robert J.[4,14]*, and Mamiko Sakata-Yanagimoto[2,5,15]*

11

12 *1 Department of Hematology, Graduate School of Comprehensive Human Sciences, University of*
13 *Tsukuba, Tsukuba, Japan.*
14 *2 Department of Hematology, Institute of Medicine, University of Tsukuba, Tsukuba, Japan.*
15 *3 Centre for Lymphoid Cancer, BC Cancer, Vancouver, BC, Canada.*
16 *4 Division of Medical Oncology and Hematology, Princess Margaret Cancer Centre, University*
17 *Health Network, Toronto, Canada*
18 *5 Department of Hematology, University of Tsukuba Hospital, Tsukuba, Japan.*
19 *6 Graduate School of Frontier Sciences, the University of Tokyo, Kashiwa, Japan.*
20 *7 Medical Institute of Bioregulation, Kyushu University, Fukuoka, Japan.*
21 *8 Division of Genetics, Cancer Research Institute, Kanazawa University, Kanazawa, Japan.*

22 *9 WPI Nano Life Science Institute, Kanazawa University, Kanazawa, Japan.*

23 *10 Department of Preventive Medicine, Graduate School of Medicine, The University of Tokyo, Tokyo,*

24 *Japan.*

25 *11 Laboratory of Clinical Genome Sequencing, Graduate School of Frontier Sciences, The University*

26 *of Tokyo, Tokyo, Japan.*

27 *12 Department of Pathology and Tumor Biology, Graduate School of Medicine, Kyoto University,*

28 *Kyoto, Japan.*

29 *13 Institute for the Advanced Study of Human Biology (WPI ASHBi), Kyoto University, Kyoto, Japan.*

30 *14 Institute of Medical Science, Temerty Faculty of Medicine, University of Toronto, Toronto,*

31 *Canada.*

32 *15 Division of Advanced Hemato-Oncology, Transborder Medical Research Center, University of*

33 *Tsukuba, Tsukuba, Japan.*

34

35 ***Correspondence:**

36 Mamiko Sakata-Yanagimoto, MD, PhD

37 Department of Hematology, Institute of Medicine, University of Tsukuba.

38 1-1-1 Tennodai, Tsukuba, Ibaraki 305-8575, Japan

39 TEL +81-29-853-3127, FAX +81-29-853-8079, E-mail: sakatama@md.tsukuba.ac.jp

40 and Robert J. Vanner, MD, PhD

41 Division of Medical Oncology and Hematology, Princess Margaret Cancer Centre,

42 University Health Network.

43 610 University Ave, Toronto, ON, Canada, M5G 2C4

44 TEL +1-416-946-4501x8673, FAX +1-416-946-6546, E-mail:

45 robert.vanner@uhn.ca

46 ***Correspondence:**

47 Mamiko Sakata-Yanagimoto, MD, PhD

48 Department of Hematology, Institute of Medicine, University of Tsukuba.

49 1-1-1 Tennodai, Tsukuba, Ibaraki 305-8575, Japan

50 TEL +81-29-853-3127, FAX +81-29-853-8079, E-mail: sakatama@md.tsukuba.ac.jp

51 and Robert J. Vanner, MD, PhD

52 Division of Medical Oncology and Hematology, Princess Margaret Cancer Centre,

53 University Health Network.

54 610 University Ave, Toronto, ON, Canada, M5G 2C4

55 TEL +1-416-946-4501x8673, FAX +1-416-946-6546, E-mail: robert.vanner@uhn.ca

56

## ABSTRACT

Clonal hematopoiesis (CH) is widely regarded as a risk factor for age-associated disease, yet its influence on solid tumor progression remains poorly understood. Here, we uncover an unexpected tumor-suppressive role for *TET2*-mutant CH in solid tumors. Through an analysis of over 16,000 cancer patients, we demonstrate that *TET2* mutations are associated with a significant reduction in metastatic burden. Mechanistically, we show that *Tet2* deficiency prevents terminal exhaustion in $CD8^+$ tumor-infiltrating lymphocytes ($CD8^+$ TILs). This resistance is driven by DNA hypermethylation at regulatory elements of the transcription factor *Tox*, which prevents the induction of the terminal exhaustion program. Consequently, *Tet2*-deficient $CD8^+$ TILs maintain stem-like, effector-competent states that mediate durable anti-tumor immunity and suppress metastatic outgrowth. Our findings establish *TET2*-mutant CH as a natural epigenetic constraint on T-cell exhaustion and uncover a mechanistically defined pathway with translational potential for enhancing anti-tumor immune responses.

## INTRODUCTION

Metastasis represents the principal cause of cancer-related mortality. Clinical metastatic disease is present in 4% to 65% of patients with solid malignancies at the time of cancer diagnosis[1]. Metastasis occurs through a complex and multi-step cascade wherein malignant cells spread beyond the primary tumor through the blood and lymph systems, colonize distant organs, and eventually manifest as metastatic lesions[2]. Immune cells recruited to metastatic sites undergo extensive reprogramming, and contribute to the formation of tumor-

79 promoting or tumor-restraining immune microenvironments[3]. Indeed, metastatic tumor-
80 infiltrating leukocytes exhibit dual effects on metastasis. Cytotoxic $CD8^+$ tumor-infiltrating
81 lymphocytes (TILs) and natural killer (NK) cells can restrain metastatic tumor cells under
82 certain conditions[4-6]. However, their anti-tumor function is frequently compromised by
83 exhaustion, characterized by upregulation of inhibitory receptors (PD-1, TIM3, LAG3) and
84 impaired effector functions within the immunosuppressive tumor microenvironment[7-9].
85 Similarly, while macrophages, neutrophils, IL-17-producing γδ T cells, and regulatory T
86 cells are commonly associated with promoting metastasis outgrowth[10-12], specific subsets
87 within these populations can exert anti-metastatic effects depending on their polarization
88 state and local microenvironmental cues. For instance, M1-polarized macrophages exhibit
89 anti-tumor activity through production of pro-inflammatory cytokines and direct
90 cytotoxicity[13,14], and presentation of tumor- antigens[15], N1-polarized neutrophils can
91 suppress tumor progression through reactive oxygen species production and immune
92 activation[16,17], and certain γδ T cell subsets demonstrate potent cytotoxic activity against
93 tumor cells and support anti-tumor immunity[18-20]. These observations indicate that the
94 phenotypic heterogeneity and functional state of tumor-infiltrating immune cells, shaped by
95 local microenvironmental cues, critically influence metastatic colonization.

96 Clonal hematopoiesis (CH), the age-associated acquisition of somatic mutations in
97 hematopoietic stem and progenitor cells, has emerged as a major source of systemic
98 inflammation and immune dysregulation. Analysis of patient samples and animal models
99 indicates that CH-derived immune cells underlie these inflammatory changes[21]. The
100 prevalence of CH in solid cancer patients is 20-30%, which is significantly higher than in

101 age-matched healthy individuals[22,23]. *DNMT3A*, *TET2*, and *ASXL1* are the most commonly
102 mutated genes driving CH in untreated solid cancer patients and in healthy individuals[23],
103 whereas exposure to cancer therapy heightens the frequency of mutations in DNA damage
104 response genes, such as *TP53*, *CHEK2,* and *PPM1D*[22]. Indeed, CH-derived mutant alleles
105 are frequently detected in tumor-infiltrating immune cells of solid cancer patients with CH[23-
106 26]. Tumor infiltration by CH-derived mutant immune cells shapes the local immune
107 microenvironment, which has been associated with tumor inflammation and poor
108 prognosis[27,28]. However, the clinical and biological implications of CH-derived immune
109 cells on solid cancer remain incompletely understood. Mouse studies revealed conflicting
110 results regarding whether CH-associated immune alterations accelerate or restrain tumor
111 growth across different cancer types[29,30]. Pan-human cancer analyses suggest CH-outcome
112 associations vary based on cancer type[22,23,31,32], and CH-driver specific outcome analyses are
113 lacking. Recently, *TET2*-mutant CH was shown to potentiate response to immune checkpoint
114 blockade in colorectal cancer (CRC), non-small cell lung cancer, melanoma, and animal
115 models[15,29,33]. Therefore, TET2 inactivation in tumor-infiltrating myeloid and lymphoid cells
116 can enhance anti-tumor immunity. Intriguingly, the potential roles of CH-derived immune
117 cells on cancer metastasis have not been clarified.

118 Here, we examined the association between CH and metastasis in a large clinical
119 cohort and further investigated how *Tet2*-deficient CH-derived immune cells regulate CRC
120 liver metastasis using conditional *Tet2* knockout mouse models.

121

122 **RESULTS**

123 ***TET2*-mutant CH is associated with lower metastatic cancer burden**

124 We analyzed CH in 16,744 non-hematological cancer patients from the MSK-IMPACT
125 cohort with matching demographic and clinical data including treatment history, cancer stage,
126 and metastatic burden[22,34]. Driver clonal hematopoiesis (CH) was defined as putative CH-
127 driver mutations with a variant allele frequency (VAF) ≥ 0.02 (Methods). Reproducing the
128 observations from the larger cohort of Bolton et al. 2020 [22], overall CH prevalence was 19.6%,
129 most commonly with *DNMT3A* (10.2%), *TET2* (3.1%), and *PPM1D* (2.6%) driver mutations
130 (Figure S1A). Prevalence increased with age, and patients with driver CH were significantly
131 older (Figures S1B and S1C). Known associations between *ASXL1* and smoking history, and
132 with *CHEK2*, *TP53*, *PPM1D* and prior exposure to cancer therapy, were recapitulated
133 (Figures S1D and S1E). Metastatic cases were more likely to have received therapy (Figure
134 S1F), and CH prevalence patterns varied by cancer type in accordance with prior studies
135 (Figures S1G and S1H).

136 To investigate a potential association between CH and cancer metastasis, we
137 compared CH prevalence in patients with and without metastatic cancer. In multivariate
138 adjusted analysis, there was a trend towards higher prevalence of driver CH in patients
139 without metastatic disease (OR 0.89, 95%CI [0.78–1.01], FDR-adjusted $P$ = 0.109, Figure
140 1A). CH with a *TET2*-driver mutation was significantly more common in patients with local
141 compared to metastatic cancers (OR 0.64, 95%CI [0.46–0.90], $P$ = 0.029; Figure 1A), while
142 *DNMT3A*-driven CH and other forms of CH with non-*DNMT3A*, non-*TET2* drivers were not
143 associated with metastatic status (Figure 1A). Non-driver somatic *TET2* variants were not
144 associated with metastatic status (Figure S1I). By cancer type, *TET2*-driver CH was

145 associated with lower odds of having metastatic breast cancer (multivariate logistic
146 regression, OR 0.36, $P = 0.022$), with similar trends in non–small cell lung cancer (NSCLC)
147 (OR 0.52, $P = 0.064$) and in CRC (OR 0.53, $P = 0.419$) (Figure 1B, Table S1). *TET2*-CH
148 was numerically but not statistically more common in patients with metastatic prostate cancer
149 (multivariate logistic regression, OR 1.98, $P = 0.419$). When examining metastatic status at
150 specific sites, patients with *TET2*-driver CH showed significantly reduced odds of having
151 liver (OR 0.67, $P = 0.016$) or brain metastasis (OR 0.54, $P = 0.016$), and showed a trend
152 towards lower odds of bone metastasis (OR 0.77, $P = 0.114$; Figure 1C).
153 When examining patients with metastatic disease**,** *TET2*-driver CH was linked to lower
154 metastatic disease burden as quantified by number of metastases (median and interquartile
155 range [IQR] metastasis number for *TET2*-CH, 3 [2-6], versus no CH and non-*TET2*-CH, 4
156 [2-7], $P = 0.035$; multivariate negative binomial generalized linear model IRR = 0.92, $P =$
157 0.052; Figures 1D and S1J) and involvement of fewer metastatic sites (median and IQR
158 metastasis site number for *TET2*-CH, 3 [2-5], versus no CH and non-*TET2*-CH, 3 [2-5], $P =$
159 0.006; multivariate negative binomial generalized linear model IRR = 0.92, $P = 0.035$; Figure
160 1E and S1K).
161 Overall, patients with driver CH mutations experienced modestly worse survival in
162 multivariate analysis (HR 1.06, $P = 0.0498$; Figure S1L). Strikingly, this was not driven by
163 *DNMT3A*- and *TET2*- driver CH (Figure 1F). While patients with *TET2*-driver CH trended
164 towards improved OS in multivariate analysis compared with no CH (HR 0.87, $P = 0.152$;
165 Figure 1F), patients with DDR- (HR 1.24, $P < 0.001$), cohesin- (HR 1.40, $P = 0.096$), and
166 spliceosome-driver CH (HR 1.30, $P = 0.034$) experienced worse survival (Figure 1F).

167 Therefore, solid tumor patients with *TET2*-CH are more likely to have local versus metastatic
168 cancer, those with metastatic cancer tend to have fewer metastases, and in contrast to other
169 forms of CH, *TET2*-mutant CH is not associated with worse overall survival. Based on these
170 results, we explored whether *TET2*-mutant CH could suppress cancer metastasis in animal
171 models.

172 Figure 1

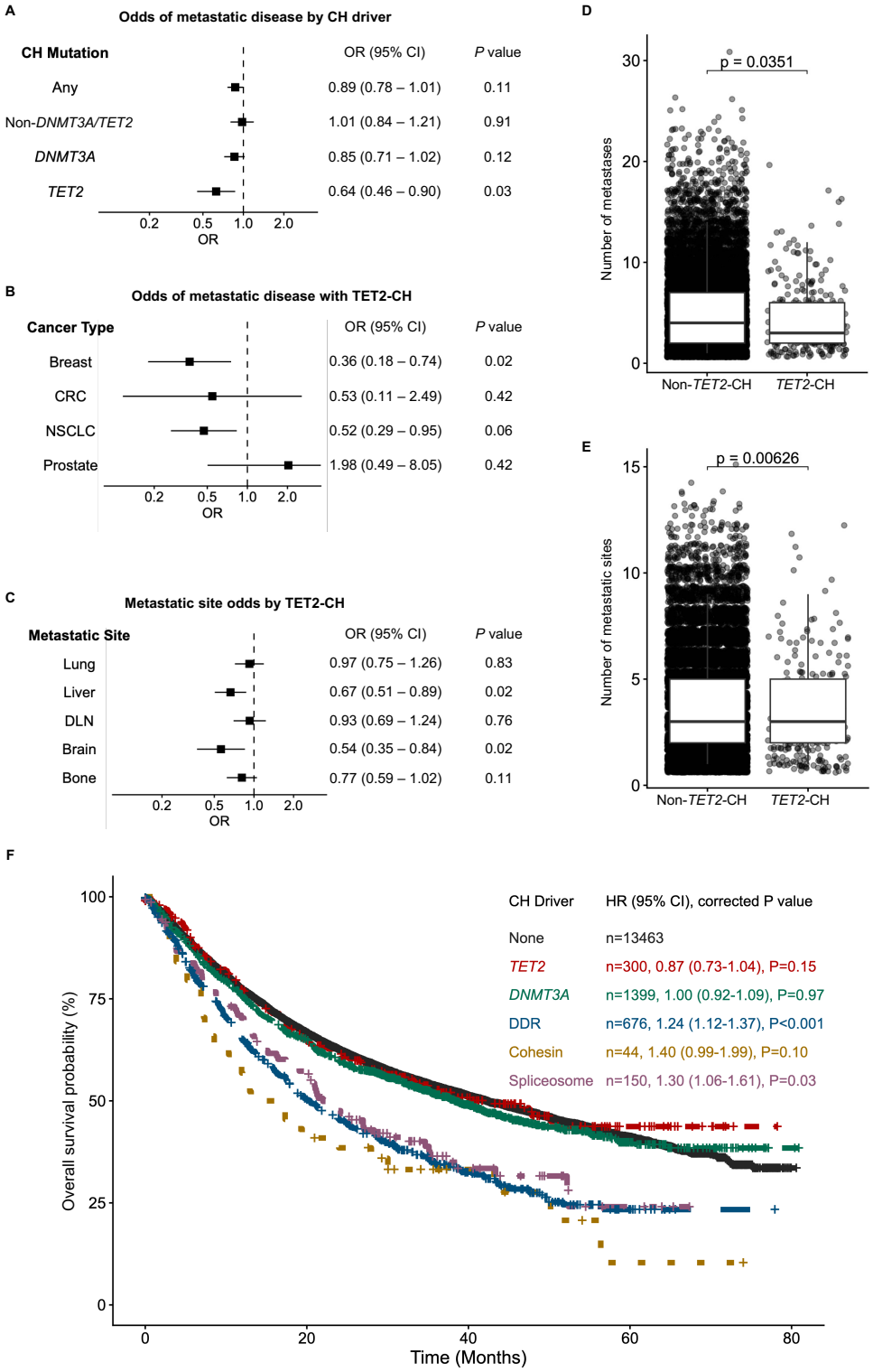
A
Odds of metastatic disease by CH driver
CH Mutation
OR (95% CI)
P value
Any
0.89 (0.78 – 1.01)
0.11
Non-DNMT3A/TET2
1.01 (0.84 – 1.21)
0.91
DNMT3A
0.85 (0.71 – 1.02)
0.12
TET2
0.64 (0.46 – 0.90)
0.03
0.2
0.5
1.0
2.0
OR
B
Odds of metastatic disease with TET2-CH
Cancer Type
OR (95% CI)
P value
Breast
0.36 (0.18 – 0.74)
0.02
CRC
0.53 (0.11 – 2.49)
0.42
NSCLC
0.52 (0.29 – 0.95)
0.06
Prostate
1.98 (0.49 – 8.05)
0.42
0.2
0.5
1.0
2.0
OR
C
Metastatic site odds by TET2-CH
Metastatic Site
OR (95% CI)
P value
Lung
0.97 (0.75 – 1.26)
0.83
Liver
0.67 (0.51 – 0.89)
0.02
DLN
0.93 (0.69 – 1.24)
0.76
Brain
0.54 (0.35 – 0.84)
0.02
Bone
0.77 (0.59 – 1.02)
0.11
0.2
0.5
1.0
2.0
OR
D
p = 0.0351
Number of metastases
0
10
20
30
Non-TET2-CH
TET2-CH
E
p = 0.00626
Number of metastatic sites
0
5
10
15
Non-TET2-CH
TET2-CH
F
Overall survival probability (%)
0
25
50
75
100
Time (Months)
0
20
40
60
80
CH Driver
HR (95% CI), corrected P value
None
n=13463
TET2
n=300, 0.87 (0.73-1.04), P=0.15
DNMT3A
n=1399, 1.00 (0.92-1.09), P=0.97
DDR
n=676, 1.24 (1.12-1.37), P<0.001
Cohesin
n=44, 1.40 (0.99-1.99), P=0.10
Spliceosome
n=150, 1.30 (1.06-1.61), P=0.03

**Figure 1. *TET2*-mutant CH is associated with reduced cancer metastasis**

(A) Adjusted odds of patient having metastatic versus local cancer by CH-mutant status with any CH-driver mutation, or stratified by (bottom) only *DNMT3A* driver, only *TET2* driver, and non-*TET2* non-*DNMT3A* mutant CH, with the reference of no CH. ORs and 95% confidence intervals are reported from logistic GLMs, and *P* values are FDR-adjusted.

(B) Adjusted odds of patient having metastatic versus local cancer given exposure to *TET2*-mutant CH for the four most prevalent cancer types. ORs and 95% confidence intervals are reported from logistic GLMs for each cancer type, and *P* values are FDR-adjusted (see also Table S1).

(C) Adjusted odds of metastasis occurring at specific sites given exposure to *TET2*-mutant CH. ORs and 95% confidence intervals are reported from logistic GLMs for each metastatic site, and *P* values are FDR-adjusted.

(D) The number of metastases in patients with metastatic cancer stratified by *TET2*-mutant CH presence. Differences in distributions are quantified both univariately by Wilcoxon rank sum tests, and multivariately adjusted with IRRs from negative binomial generalized linear models (Supplementary Figure1J).

(E) The distribution of the number of metastatic sites in patients with metastatic cancer stratified by *TET2*-mutant CH presence. Differences in distributions are quantified both univariately by Wilcoxon rank sum tests, and multivariately adjusted with IRRs from negative binomial generalized linear models (Supplementary Figure1K).

(F) Kaplan-Meier (KM) survival curves for overall survival of all patients, stratified by no CH mutation, and *DNMT3A*-, *TET2*-, DNA-damage-response (DDR)-, cohesin-, and spliceosome-mutant CH. Adjusted hazard ratios (HR) are reported from a Cox proportional hazards model, with the reference of no CH, and *P* values are FDR-adjusted.

CH, clonal hematopoiesis; OR, Odds ratio; GLM, generalized linear model; FDR, false discovery rate; IRR, incidence risk ratio. Detailed statistical outputs, test statistics, and model parameters for all panels in Figure 1 are provided in Table S2.

173

174 ***Tet2* deficiency in T cells inhibits CRC liver metastasis in mice**

175 We investigated the effects of hematopoietic *Tet2* deficiency on CRC metastasis to the liver,
176 since *TET2*-CH was prominently associated with reduced metastasis to this site (Figure 1C)
177 and CRC is one of the most common causes of liver metastasis. To explore the role *of Tet2*
178 loss of function in different types of immune cells on CRC metastasis, we crossed mice
179 carrying *LoxP*-flanked *Tet2* alleles ($Tet2^{fl/fl}$)[35] with $Vav1^{Cre}$ [36], $Cd4^{Cre}$ [37], $Cd19^{Cre}$ [38], and
180 $LysM^{Cre}$ [39] to generate mice with targeted *Tet2* knockout (KO) in all hematopoietic cells
181 ($Vav1^{Cre}Tet2KO$ mice), B lymphoid cells ($Cd19^{Cre}Tet2KO$ mice), T lymphoid cells
182 ($Cd4^{Cre}Tet2KO$ mice), and myeloid cells ($LysM^{Cre}Tet2KO$ mice), respectively. Venus-
183 labeled mouse intestinal tumor-derived organoid cells carrying $Apc^{\Delta 716}$, $Kras^{+/G12D}$, $Tgfbr2^{-}$
184 $^{/-}$ and $Trp^{R270H/LOH}$ mutations (Venus-$AKTP^{M/LOH}$ cells)[40], which acquired the ability to
185 metastasize to the liver, were injected into the spleen of various *Tet2* conditional KO mice
186 and $Tet2^{fl/fl}$ mice to generate CRC liver metastases (Figure 2A). After 30 days, liver metastatic
187 tumor burden (LMTB) was lower in $Vav1^{Cre}Tet2KO$ mice and $Cd4^{Cre}Tet2KO$ mice than in
188 $Tet2^{fl/fl}$ mice, while LMTB of $Cd19^{Cre}Tet2KO$ and $LysM^{Cre}Tet2KO$ mice was comparable
189 with that of $Tet2^{fl/fl}$ mice (Figures 2B and 2C; Table S3). This result suggests that *Tet2*
190 deficiency in T cells, but not in B cells or myeloid cells, is sufficient to restrict CRC liver
191 metastasis in mice.

192 Figure 2

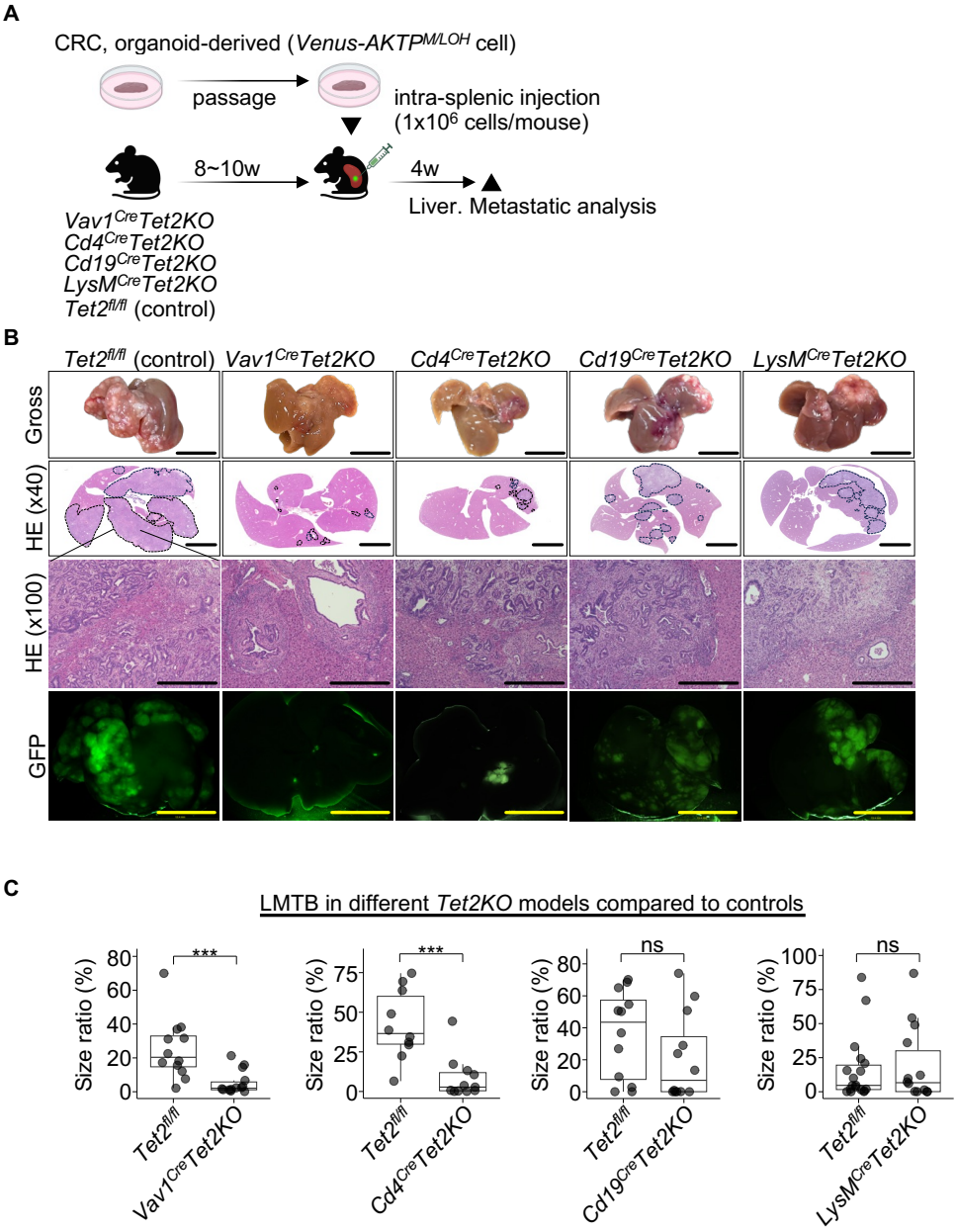
A
CRC, organoid-derived (Venus-AKTP M/LOH cell)
passage
intra-splenic injection
(1x10^6 cells/mouse)
8~10w
4w
Liver. Metastatic analysis
Vav1 Cre Tet2KO
Cd4 Cre Tet2KO
Cd19 Cre Tet2KO
LysM Cre Tet2KO
Tet2 fl/fl (control)
B
Tet2 fl/fl (control)
Vav1 Cre Tet2KO
Cd4 Cre Tet2KO
Cd19 Cre Tet2KO
LysM Cre Tet2KO
Gross
HE (x40)
HE (x100)
GFP
C
LMTB in different Tet2KO models compared to controls
Size ratio (%)
***
ns
Tet2 fl/fl
Vav1 Cre Tet2KO
Cd4 Cre Tet2KO
Cd19 Cre Tet2KO
LysM Cre Tet2KO

**Figure 2. *Tet2* deficiency in T cells, but not in myeloid and B cells, inhibits the liver metastasis of CRC in mice.**

(A) Schematic of the CRC liver metastasis model using cell-type-specific *Tet2* knockout mice. CRC organoid-derived Venus-*AKTP*$^{M/LOH}$ cells ($1\times10^6$ cells/mouse) were intrasplenically injected into *Vav1*$^{Cre}$*Tet2KO, Cd4*$^{Cre}$*Tet2KO*, *Cd19*$^{Cre}$*Tet2KO*, *LysM*$^{Cre}$*Tet2KO*, and *Tet2*$^{fl/fl}$ control mice. Liver metastases were analyzed 4 weeks post-injection.

(B) Representative macroscopic (top row), HE-stained (middle rows; 40× and 100× magnification), and GFP fluorescence (bottom row) images of liver metastases. Scale bars: 1 cm (macroscopic and GFP); 5 mm (HE, 40×); 500 µm (HE, 100×).

(C) Quantification and comparisons of LMTB between different Tet2KO models and *Tet2*$^{fl/fl}$ controls. See also Table S3 for detailed quantification and statistical comparisons.

CRC, colorectal cancer; HE, hematoxylin and eosin; GFP, green fluorescent protein; LMTB, liver metastatic tumor burden. Data in (C) are pooled from 3 independent experiments (total $n$ = 11-14 mice per group). Statistical significance was determined by Mann-Whitney U test. *$p < 0.05$, **$p < 0.01$, ***$p < 0.001$, ****$p < 0.0001$, ns = not significant.

193

194 ***Tet2* deficiency reshapes CD8$^+$ TILs through the *Tox*-exhaustion axis to enhance anti-**
195 **tumor immunity**

196 To determine which T cell subsets are regulated by *Tet2* in the anti-tumor response, we
197 compared the transcriptional profiles of CD4$^+$ TILs and CD8$^+$ TILs isolated from CRC liver
198 metastases of *Vav1$^{Cre}$Tet2KO* mice, *Cd4$^{Cre}$Tet2KO* mice, and *Tet2$^{fl/fl}$* mice (Figure 3A).
199 Principal component analysis (PCA) and heatmap clustering showed that biological
200 replicates of CD8$^+$ TILs from either *Vav1$^{Cre}$Tet2KO* mice or *Cd4$^{Cre}$Tet2KO* mice
201 (*Vav1$^{Cre}$/Cd4$^{Cre}$Tet2KO* CD8$^+$ TILs) clustered closely together but distinctly from their
202 *Tet2$^{fl/fl}$* counterparts, while *Tet2KO* CD4$^+$ TILs showed no significant separation from *Tet2$^{fl/fl}$*
203 CD4$^+$ TILs (Figures 3B and S2A, Table S4). Comparing *Vav1$^{Cre}$/Cd4$^{Cre}$Tet2KO* groups to
204 *Tet2$^{fl/fl}$* group identified substantially more differentially expressed genes (DEGs) in CD8$^+$
205 TILs than in CD4$^+$ TILs (Figure 3C). In the *Vav1$^{Cre}$Tet2KO* model, CD8$^+$ TILs exhibited 226
206 DEGs compared to 71 DEGs in CD4$^+$ TILs. This disparity was even more pronounced in the
207 *Cd4$^{Cre}$Tet2KO* model, where CD8$^+$ TILs demonstrated 209 DEGs versus only 8 DEGs in
208 CD4$^+$ TILs (FDR$<$ 0.01, |Log2 FC| $>$ 2) (Figure 3C, Table S5-S8). These findings suggest
209 that *Tet2* deficiency affects the transcriptome of CD8$^+$ TILs more than CD4$^+$ TILs.

210 Notably, multiple exhaustion-associated genes including *Pdcd1*, *Lag3*, *Tim3*, *Tigit*,
211 *Prdm1*, *Tnfrsf9*, and *Tox* were the most significantly downregulated genes in
212 *Vav1$^{Cre}$/Cd4$^{Cre}$Tet2KO* CD8$^+$ TILs relative to *Tet2$^{fl/fl}$* CD8$^+$ TILs, suggesting attenuated
213 exhaustion programs in the absence of *Tet2*. (Figure 3D; Table S5 and S6). In CD8$^+$ TILs,
214 DEG analysis showed substantial concordance between *Vav1$^{Cre}$Tet2KO* and *Cd4$^{Cre}$Tet2KO*
215 models with 198 commonly upregulated and 89 commonly downregulated genes, including

216 downregulation of exhaustion markers *Tox* and *Pdcd1* (FDR< 0.05, |Log2 FC| > 1) (Figure
217 S2B). Using DAVID gene functional classification[41], we clustered 89 overlapping
218 downregulated genes shared by *Vav1*$^{Cre}$*Tet2KO* CD8$^{+}$ TILs and *Cd4*$^{Cre}$*Tet2KO* CD8$^{+}$ TILs
219 compared to *Tet2*$^{fl/fl}$ CD8$^{+}$ TILs (Table S9A). Under stringent parameters (Table S9B), these
220 consistently downregulated genes were classified into a single cluster comprising six genes
221 associated with immunologic function, with an enrichment score of 2.59 (Figure 3E). Notably,
222 this downregulated cluster encompassed key genes linked to T-cell exhaustion, including
223 *Pdcd1*, *Lag3*, and *Tigit* (Figure 3E; Table S9C).

224 Gene Set Enrichment Analysis (GSEA)[42] was performed using the ImmuneSigDB
225 subset C7 from the Molecular Signatures Database (MSigDB)[43] to compare the genome
226 expression profiles of *Tet2KO* CD8$^{+}$ TILs and *Tet2*$^{fl/fl}$ CD8$^{+}$ TILs. The analysis identified 92
227 gene sets significantly enriched in *Tet2*$^{fl/fl}$ CD8$^{+}$ TILs compared to *Cd4*$^{Cre}$*Tet2KO* CD8$^{+}$ TILs,
228 five of which were specifically associated with T-cell exhaustion (Figures 3F and S3A; Table
229 S10). In the same approach, 51 gene sets related to CD8 T-cell function were enriched in
230 *Tet2*$^{fl/fl}$ CD8$^{+}$ TILs compared to *Vav1*$^{Cre}$*Tet2KO* CD8$^{+}$ TILs, including five exhaustion-
231 associated signatures (Figures 3F and S3A, Table S11). Of the 34 gene sets consistently
232 enriched in *Tet2*$^{fl/fl}$ CD8$^{+}$ TILs relative to both *Vav1*$^{Cre}$*Tet2KO* and *Cd4*$^{Cre}$*Tet2KO*
233 counterparts, four were linked to T-cell exhaustion (Figure S3B).

234 Ingenuity Pathway Analysis (IPA) of 89 consistently downregulated genes in
235 *Vav1*$^{Cre}$*Tet2KO* CD8$^{+}$ TILs and *Cd4*$^{Cre}$*Tet2KO* CD8$^{+}$ TILs (Table S12) identified the
236 transcription factor *Tox* as one of the potential upstream regulators targeting genes associated
237 with T-cell exhaustion (overlap *p*-value = 0.00164) (Figure 3G; Table S12). Consistent with

238 this finding, *Tox* exhibited the greatest differential expression with the lowest *P* value among
239 all tested genes, with levels markedly higher in *Tet2*$^{fl/fl}$ CD8$^{+}$ TILs compared to
240 *Vav1*$^{Cre}$/*Cd4*$^{Cre}$*Tet2KO* CD8$^{+}$ TILs (*Tet2*$^{fl/fl}$ vs. *Vav1*$^{Cre}$*Tet2KO*, $P$ = 0.0002; *Tet2*$^{fl/fl}$ vs.
241 *Cd4*$^{Cre}$*Tet2KO*, $P$ = 0.0001; Figure S3C; Table S13).

242 Furthermore, flow cytometry analysis of CRC metastatic tumors in the liver revealed
243 a significantly higher percentage of CD8$^{+}$ TILs co-expressing exhaustion markers Tim3 and
244 PD-1 of the *Tet2*$^{fl/fl}$ group compared with that of the *Vav1*$^{Cre}$/*Cd4*$^{Cre}$*Tet2KO* group (Figure
245 S4A; Table S14A). Indirect immunofluorescence staining further demonstrated a higher
246 number of CD8α cells co-expressing Tim3, PD-1 and Tox in tumors from the *Tet2*$^{fl/fl}$ group
247 than in the *Vav1*$^{Cre}$/*Cd4*$^{Cre}$*Tet2KO* groups (Figure S4B; Table S14B). Collectively, these
248 findings identify *Tet2* as a critical enforcer of the terminal exhaustion program, which is
249 intrinsically linked to high *Tox* expression.

250 To further validate the role of *Tet2* in regulating the antitumor functions of CD8$^{+}$
251 TILs, we performed CD8 T-cell depletion experiments in *Cd4*$^{Cre}$*Tet2KO* and *Tet2*$^{fl/fl}$ mice
252 (Figure 3H). Circulating and liver-infiltrating CD8 T cells were efficiently and specifically
253 depleted in anti-CD8α antibody-treated groups compared with PBS controls (Figures S5A
254 and S5B). CD8 T-cell depletion in *Cd4*$^{Cre}$*Tet2KO* mice drastically increased LMTB
255 compared to their PBS-treated controls ($P$ = 0.007), while CD8 T-cell depletion in *Tet2*$^{fl/fl}$
256 mice had no significant effect ($P$ = 0.396) (Figures 3I, 3J and S5C; Table S15). As a result,
257 LMTB of anti-CD8α antibody-treated *Cd4*$^{Cre}$*Tet2KO* mice was not significantly different
258 from that of anti-CD8α antibody-treated *Tet2*$^{fl/fl}$ mice ($P$ = 1.0) and was comparable to that
259 of PBS-treated *Tet2*$^{fl/fl}$ mice ($P$ = 1.0), indicating that CD8 T-cell depletion attenuated the

260 tumor-restrictive effect observed in *Tet2*-deficient mice (Figures 3I, 3J and S5C; Table S15).
261 In contrast, PBS-treated $Cd4^{Cre}Tet2KO$ mice revealed a significantly lower LMTB compared
262 to PBS-treated $Tet2^{fl/fl}$ mice ($P$ = 0.007) (Figures 3I, 3J and S5C; Table S15), consistent with
263 our earlier results. Collectively, these data demonstrate that the enhanced tumor control
264 observed in *Cd4CreTet2KO* mice requires $CD8^+$ TILs.

265 Figure 3

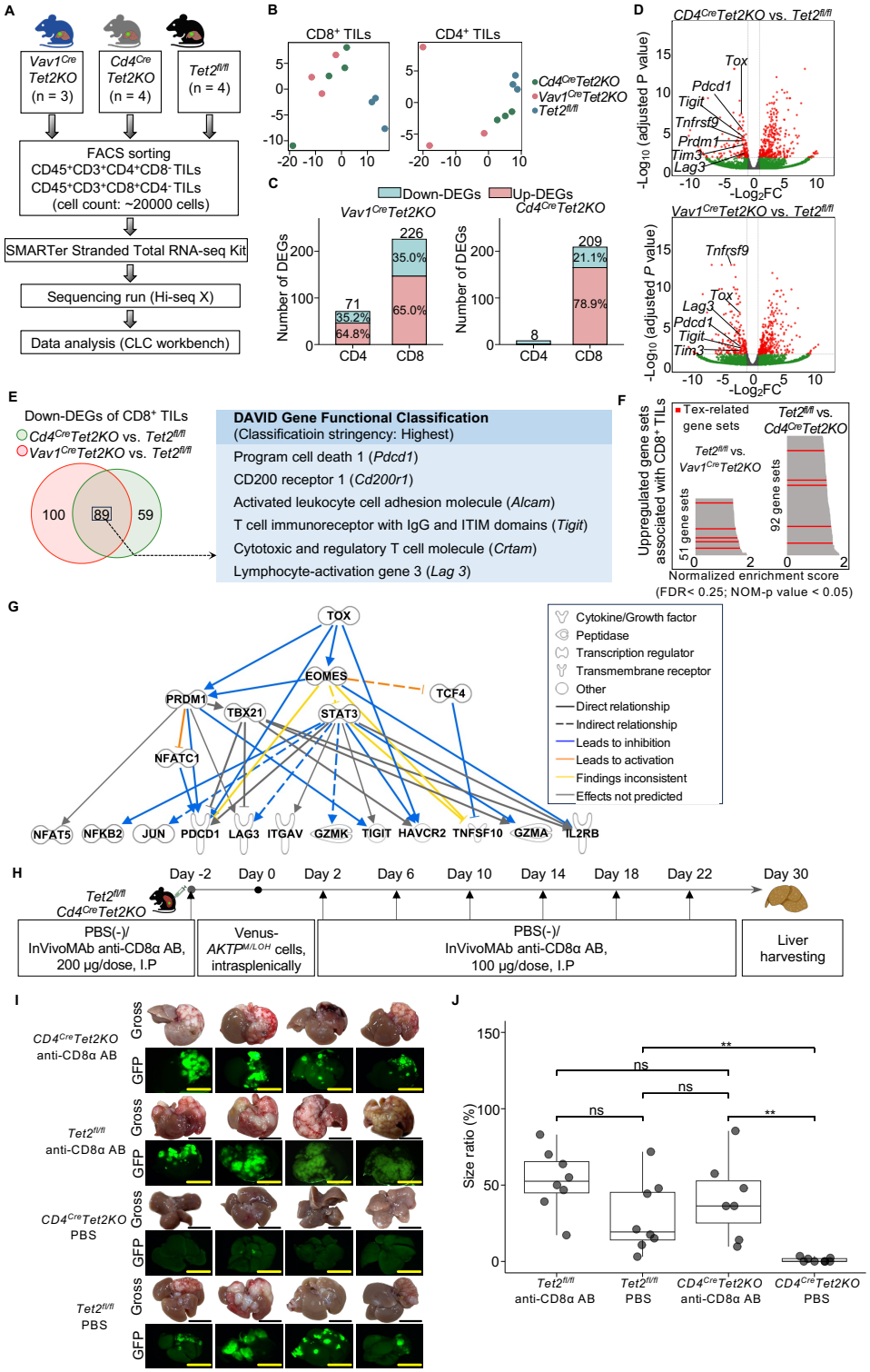
A
Vav1Cre Tet2KO (n = 3)
Cd4Cre Tet2KO (n = 4)
Tet2fl/fl (n = 4)
FACS sorting
CD45+CD3+CD4+CD8- TILs
CD45+CD3+CD8+CD4- TILs
(cell count: ~20000 cells)
SMARTer Stranded Total RNA-seq Kit
Sequencing run (Hi-seq X)
Data analysis (CLC workbench)
B
CD8+ TILs
CD4+ TILs
Cd4CreTet2KO
Vav1CreTet2KO
Tet2fl/fl
C
Down-DEGs
Up-DEGs
Vav1CreTet2KO
Cd4CreTet2KO
Number of DEGs
71
35.2%
64.8%
226
35.0%
65.0%
8
209
21.1%
78.9%
CD4
CD8
D
CD4CreTet2KO vs. Tet2fl/fl
Vav1CreTet2KO vs. Tet2fl/fl
-Log10 (adjusted P value)
-Log2FC
Tox
Pdcd1
Tigit
Tnfrsf9
Prdm1
Tim3
Lag3
E
Down-DEGs of CD8+ TILs
Cd4CreTet2KO vs. Tet2fl/fl
Vav1CreTet2KO vs. Tet2fl/fl
100
89
59
DAVID Gene Functional Classification
(Classificatioin stringency: Highest)
Program cell death 1 (Pdcd1)
CD200 receptor 1 (Cd200r1)
Activated leukocyte cell adhesion molecule (Alcam)
T cell immunoreceptor with IgG and ITIM domains (Tigit)
Cytotoxic and regulatory T cell molecule (Crtam)
Lymphocyte-activation gene 3 (Lag 3)
F
Tex-related gene sets
Tet2fl/fl vs. Cd4CreTet2KO
Tet2fl/fl vs. Vav1CreTet2KO
Upregulated gene sets associated with CD8+ TILs
51 gene sets
92 gene sets
Normalized enrichment score
(FDR< 0.25; NOM-p value < 0.05)
G
TOX
EOMES
TCF4
PRDM1
TBX21
STAT3
NFATC1
NFAT5
NFKB2
JUN
PDCD1
LAG3
ITGAV
GZMK
TIGIT
HAVCR2
TNFSF10
GZMA
IL2RB
Cytokine/Growth factor
Peptidase
Transcription regulator
Transmembrane receptor
Other
Direct relationship
Indirect relationship
Leads to inhibition
Leads to activation
Findings inconsistent
Effects not predicted
H
Tet2fl/fl
Cd4CreTet2KO
Day -2
Day 0
Day 2
Day 6
Day 10
Day 14
Day 18
Day 22
Day 30
PBS(-)/ InVivoMAb anti-CD8α AB, 200 μg/dose, I.P
Venus-AKTPM/LOH cells, intrasplenically
PBS(-)/ InVivoMAb anti-CD8α AB, 100 μg/dose, I.P
Liver harvesting
I
CD4CreTet2KO anti-CD8α AB
Tet2fl/fl anti-CD8α AB
CD4CreTet2KO PBS
Tet2fl/fl PBS
Gross
GFP
J
Size ratio (%)
ns
**
Tet2fl/fl anti-CD8α AB
Tet2fl/fl PBS
CD4CreTet2KO anti-CD8α AB
CD4CreTet2KO PBS

**Figure 3. *Tet2* deficiency extensively reshapes CD8$^+$ TILs transcriptional profiles through the *Tox*-exhaustion axis to enhance anti-tumor immunity in CRC liver metastasis.**

(A) Schematic of the experimental workflow for transcriptomic profiling. CD45$^+$ tumor-infiltrating leukocytes were isolated via MACS and sorted by FACS into CD4$^+$ and CD8$^+$ T cells, respectively. Total RNA was extracted from sorted populations and subjected to library preparation using SMARTer Stranded Total RNA-seq Kit, followed by high-throughput sequencing (Hi-seq X) and data analysis (CLC workbench).

(B) PCA plots of CD4 and CD8$^+$ TILs supervised by the top 200 DEGs. Gene ranking was based on combined FDR calculated by multiplying the two individual FDR from *Vav1$^{Cre}$Tet2KO* vs. *Tet2$^{fl/fl}$* FDR and *Cd4$^{Cre}$Tet2KO* vs. *Tet2$^{fl/fl}$* comparisons (selection criteria: FDR < 0.05, |Log2 FC| > 1 in both comparisons) (see also Table S4).

(C) Stacked bar plots show the number of upregulated and downregulated genes in CD4 and CD8$^+$ TILs from the comparison between *Vav1$^{Cre}$/Cd4$^{Cre}$Tet2KO* groups to *Tet2$^{fl/fl}$* group (FDR < 0.01, |Log2 FC| > 2).

(D) Volcano plots show DEGs of *Vav1$^{Cre}$/Cd4$^{Cre}$Tet2KO* CD8$^+$ TILs in comparison with *Tet2$^{fl/fl}$* CD8$^+$ TILs (FDR < 0.05, |Log2 FC| > 1).

(E) Venn diagrams display 89 overlapping down-DEGs in the comparison between *Vav1$^{Cre}$Tet2KO* and *Cd4$^{Cre}$Tet2KO* with *Tet2$^{fl/fl}$* CD8$^+$ TILs (FDR < 0.05, Log2 FC < -1). Also shown is the DAVID functional classification of these overlapping genes, highlighting a cluster associated with immunologic function (Enrichment Score: 2.59; stringent parameters).

(F) GSEA using ImmuneSigDB subset of C7 showing the enrichment of T-cell exhaustion-related signatures in *Tet2$^{fl/fl}$* CD8$^+$ TILs relative to *Vav1$^{Cre}$/Cd4$^{Cre}$Tet2KO* CD8$^+$ TILs (FDR < 0.25, nominal $p < 0.05$).

(G) Interaction network of *Tox* and T-cell exhaustion-related genes identified by IPA. The analysis was based on the 89 overlapping down-DEGs within CD8$^+$ TILs from *Vav1$^{Cre}$Tet2KO* and *Cd4$^{Cre}$Tet2KO* groups compared to the *Tet2$^{fl/fl}$* groups (FDR < 0.05, Log2 FC < -1).

(H) Schematic of the CD8 T-cell depletion experiment. Venus-*AKTP$^{M/LOH}$* cells were intrasplenically transplanted into *Cd4$^{Cre}$Tet2KO* or *Tet2$^{fl/f}$* mice. Anti-CD8α antibody or PBS was initiated 2 days before transplantation, and continued every 4 days throughout tumor progression.

(I) Representative macroscopic and GFP fluorescence images of liver metastases 30 days post-injection. Scale bars, 1 cm.

(J) Quantification of LMTB based on the ratio of tumor area to total liver area (%) See also Table S15 for detailed quantification and statistical comparisons.

TILs, tumor-infiltrating lymphocytes; CRC, colorectal cancer; MACS, magnetic-activated cell sorting; FACS, fluorescence-activated cell sorting; PCA, principal component analysis; DEG, differentially expressed gene; GSEA, Gene Set Enrichment Analysis; IPA, Ingenuity Pathway Analysis; GFP, green fluorescent protein; LMTB, liver metastatic tumor burden; PBS, phosphate-buffered saline. Data in (J) are compiled of 2 independent experiments (total $n$ = 7-8 mice per group). Statistical significance in (J) was determined by pairwise Mann-Whitney U tests with Bonferroni correction for multiple comparisons. *$P < 0.05$, **$P < 0.01$, ***$P < 0.001$, ****$P < 0.0001$, ns = not significant.

266

267 ***Tet2* deficiency preserves effector function and restricts terminal differentiation of**
268 **CD8$^+$ TILs**

269 To comprehensively characterize the transcriptional landscape of *Tet2*-deficient CD8$^+$ TILs,
270 we performed single cell RNA sequencing (scRNA-seq) with V(D)J profiling. We profiled
271 16,790 and 17,367 CD45$^+$ tumor-infiltrating leukocytes isolated from liver metastatic tumors
272 of *Tet2$^{fl/fl}$* ($n$ = 2) and *Vav1$^{Cre}$Tet2KO* ($n$ = 2), respectively (Figure S6A). CD8$^+$ TIL clusters
273 were identified *in silico* from CD45$^+$ tumor-infiltrating leukocytes (Figures S6B-S6J). *In*
274 *silico*-defined CD8$^+$ TILs were subjected to unsupervised sub-clustering, resulting in the
275 identification of 9 distinct clusters, consisting of stem-like CD8 T cells ($T_{SLC}$, *Ly6c2$^{low}$*CD8
276 $T_{SLC}$ and *Ly6c2$^{high}$*CD8 $T_{SLC}$), precursor/progenitor T cells ($T_{PROG}$), cytotoxic/effector-like
277 exhausted T cells ($T_{EFF-1}$ and $T_{EFF-2}$), intermediate exhausted T cells ($T_{INT-1}$ and $T_{INT-2}$),
278 terminally exhausted T cells ($T_{TEX}$), and proliferative exhausted T cells (P-$T_{EX}$) (Figures 4A
279 and 4B). $T_{PROG}$ was characterized by the high expression of stem-like T-cell markers (*Sell*,
280 *Ccr7*, *Tcf7*, *Il7r* and *Id3*) along with the dual expression of effector-like and exhausted T-cell
281 markers at moderate or low levels (Figure 4C, Table S16). $T_{EFF}$ (T4 and T5) cells displayed
282 moderate to high expression of cytolytic/effector-like and exhaustion markers. $T_{TEX}$ (T8) cells
283 were defined by the high expression of multiple exhaustion markers and reduced expression
284 in effector-like markers (Figure 4C, Table S16). Among the spectrum of CD8$^+$ TILs, $T_{PROG}$
285 (T3) and $T_{EFF}$ (T4 and T5) were predominant in *Vav1$^{Cre}$Tet2KO* mice, while $T_{INT}$ (T6 and
286 T7), $T_{TEX}$ (T8) and P-$T_{EX}$ (T9) were dominant in control *Tet2$^{fl/fl}$* mice (Figure 4B). Among
287 stem-like CD8$^+$ TILs, *Ly6c2$^{high}$*$T_{SLC}$ (T2) was markedly enriched in *Tet2$^{fl/fl}$* compared to
288 *Vav1$^{Cre}$Tet2KO* mice (Figure 4B). DEG analysis revealed significant upregulation of

289 exhaustion-associated genes, including *Tox, Tim3, Tnfrsf9, Eomes,* and *Gzmk*, in *Tet2*$^{fl/fl}$
290 CD8$^+$ TILs comparing to *Tet2KO* CD8$^+$ TILs, consistent with bulk RNA-seq data (Figure
291 4D; Table S17). In contrast, cytolytic and effector-related genes, such as *Klrc1, Klrk1, Ifng,*
292 *Tnf, Cd160, Ly6a, Cxcr3, Id2, Nr4a,* and *Ccl4*, were significantly upregulated in *Tet2KO*
293 CD8$^+$ TILs (Figure 4D; Table S17). Gene-set activity measured by AUCell scoring[44] further
294 demonstrated significant enrichment of effector-versus exhausted-T-cell signatures ($p$ =
295 0.013), as well as memory- versus exhausted-T-cell signatures ($p < 0.0001$), in *Tet2KO* CD8$^+$
296 TILs compared with *Tet2*$^{fl/fl}$ CD8$^+$ TILs (Figure 4E).

297 To characterize the exhaustion phenotype, we analyzed the expression of a signature
298 comprising 42 genes consistently associated with exhausted T cells[45] (Table S18) via
299 heatmap analysis (Figure 4F). $T_{SLC}$ (T1 and T2) clusters exhibited lower average expression
300 of most exhaustion-associated markers, consistent with their progenitor state. In contrast,
301 $T_{TEX}$ (T8) and P-$T_{EX}$ (T9) clusters displayed high expression across multiple exhaustion
302 markers (Figure 4F). Notably, 32 out of the 42 exhaustion-associated genes were highly
303 expressed in *Tet2*$^{fl/fl}$ CD8$^+$ TILs but downregulated in *Vav1*$^{Cre}$*Tet2KO* CD8$^+$ TILs (Figure
304 4F). To quantify this, we calculated the exhaustion score using this 42 gene signature. The
305 T-cell exhaustion score delineated the spectrum of exhausted T cells with positive scoring
306 values increasing toward the $T_{TEX}$ cluster (Figure 4G). *Tet2*$^{fl/fl}$ CD8$^+$ TILs exhibited a
307 significantly higher exhaustion score than *Tet2KO* CD8$^+$ TILs (Figure 4H).

308 Using *Monocle 3*[46], we reconstructed the pseudotime trajectory of CD8$^+$ TILs to
309 investigate differentiation dynamics within the metastatic tumor microenvironment (Figure
310 4I). *Ly6c2*$^{low}$$T_{SLC}$ cells were located at the root of the trajectory, consistent with their

311 progenitor-like identity. Along this trajectory, $T_{PROG}$ cells differentiated toward $T_{EFF-1}$ or
312 diverged toward $T_{TEX}$ after transitioning through $T_{INT}$ states. A subset of $T_{EFF-1}$ cells retained
313 cytolytic capacity as inferred by effector signatures and progressed into $T_{EFF-2}$, while others
314 gradually lost effector function and transitioned to $T_{TEX}$ (Figure 4I). We next examined the
315 T-cell receptor (TCR) clonotype landscape using strict clonotype calling based on the
316 combination of V(D)J genes and the nucleotide sequence of the CDR3 region[47] (Figure 4J).
317 Clonal expansion states were classified by TCR clone size: single (1 cell), small (2–5 cells),
318 medium (6–20 cells), large (21–100 cells), and hyperexpanded (>100 cells). Hyperexpanded
319 clones were predominantly enriched within $T_{INT}$ and $T_{TEX}$ clusters of *Tet2*$^{fl/fl}$ CD8$^{+}$ TILs,
320 reflecting a biased differentiation toward terminal exhaustion (Figures 4J, S7A and S7B).

321 Clonal structure analysis revealed significantly greater repertoire diversity in Tet2KO
322 mice, whereas *Tet2*$^{fl/fl}$ mice exhibited marked oligoclonal dominance, particularly within
323 exhausted T cell states (Figures S7C and S7D). Clone size distribution across differentiation
324 states demonstrated that hyperexpanded clones in *Tet2*$^{fl/fl}$ were predominantly concentrated
325 in exhaustion states ($T_{INT}$ [T6-T7], $T_{TEX}$ [T8], and P-$T_{EX}$ [T9]), while medium and large
326 clones were underrepresented in effector states ($T_{EFF-1}$ and $T_{EFF-2}$ [T4-T5]). Conversely,
327 *Tet2KO* CD8$^{+}$ TILs displayed more balanced clone size distribution (Figures 4J and S7E-
328 S7F).

329 The TCR clonotype overlap analysis highlighted distinct differences in differentiation
330 dynamics between *Tet2*$^{fl/fl}$ and *Tet2KO* CD8$^{+}$ TILs. In *Tet2*$^{fl/fl}$ CD8$^{+}$ TILs, there was an
331 absence of TCR overlap between the progenitor-like states (*Ly6c2*$^{high}$ $T_{SLC}$ [T2] and $T_{PROG}$
332 [T3]) and cytolytic/effector states ($T_{EFF-1}$ [T4] and $T_{EFF-2}$ [T5]), indicating a restricted clonal

333 relationship (Figure 4K). Conversely, *Tet2KO* CD8$^{+}$ TILs exhibited robust TCR overlap
334 among these populations (Figure 4K). Collectively, these data demonstrate that *Tet2*
335 deficiency prevents the oligoclonal expansion of terminally exhausted clones, while
336 preserving a broad and diverse TCR repertoire across the progenitor and effector states.

337 Figure 4

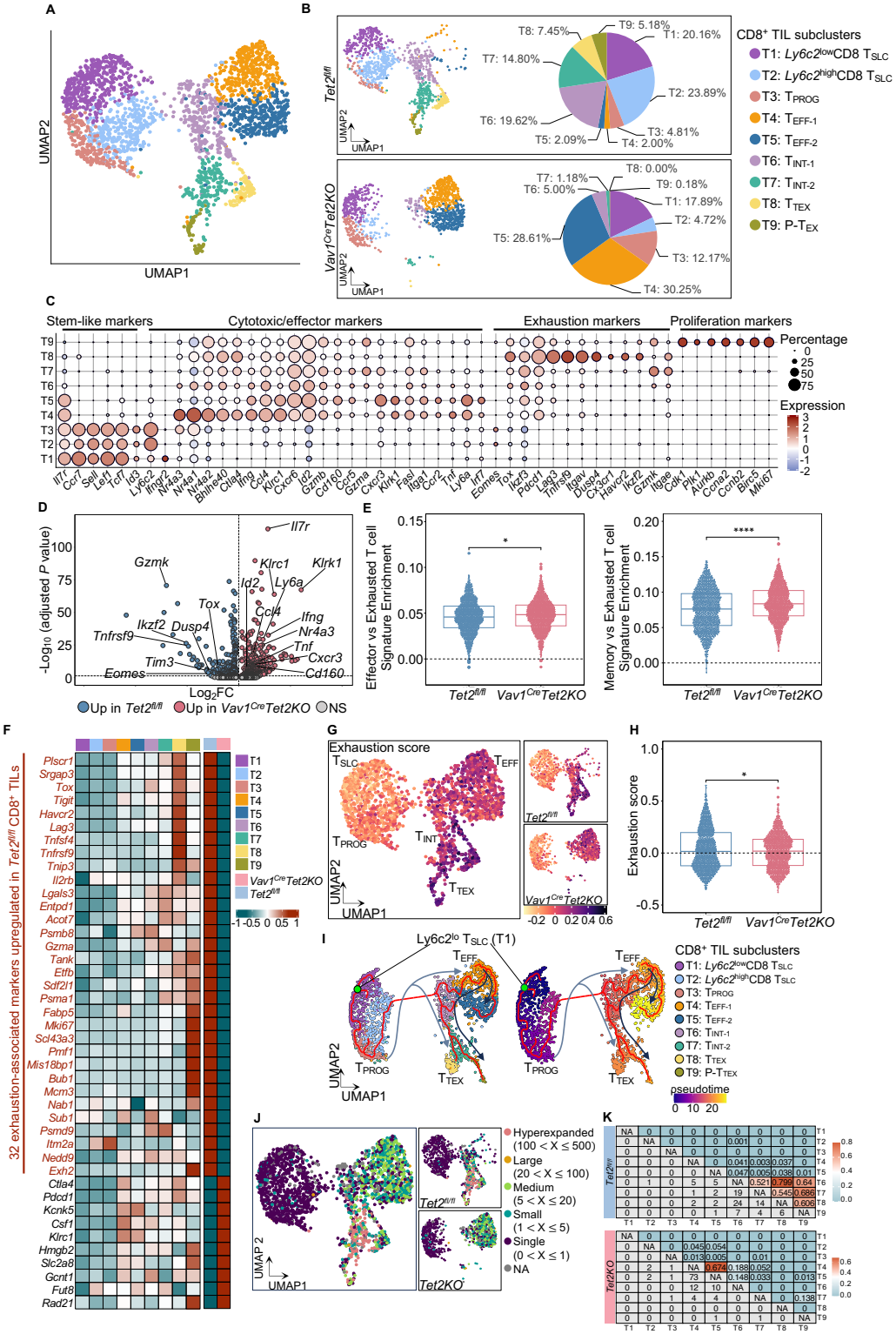
A
UMAP2
UMAP1
B
Tet2fl/fl
Vav1CreTet2KO
T8: 7.45%
T9: 5.18%
T1: 20.16%
T7: 14.80%
T2: 23.89%
T6: 19.62%
T3: 4.81%
T5: 2.09%
T4: 2.00%
T7: 1.18%
T8: 0.00%
T6: 5.00%
T9: 0.18%
T1: 17.89%
T2: 4.72%
T5: 28.61%
T3: 12.17%
T4: 30.25%
CD8+ TIL subclusters
T1: Ly6c2lowCD8 TSLC
T2: Ly6c2highCD8 TSLC
T3: TPROG
T4: TEFF-1
T5: TEFF-2
T6: TINT-1
T7: TINT-2
T8: TTEX
T9: P-TEX
C
Stem-like markers
Cytotoxic/effector markers
Exhaustion markers
Proliferation markers
Percentage
Expression
D
-Log10 (adjusted P value)
Log2FC
Up in Tet2fl/fl
Up in Vav1CreTet2KO
NS
E
Effector vs Exhausted T cell Signature Enrichment
Memory vs Exhausted T cell Signature Enrichment
Tet2fl/fl
Vav1CreTet2KO
F
32 exhaustion-associated markers upregulated in Tet2fl/fl CD8+ TILs
G
Exhaustion score
H
Exhaustion score
I
Ly6c2lo TSLC (T1)
pseudotime
J
Hyperexpanded (100 < X ≤ 500)
Large (20 < X ≤ 100)
Medium (5 < X ≤ 20)
Small (1 < X ≤ 5)
Single (0 < X ≤ 1)
NA
K
Tet2fl/fl
Tet2KO

**Figure 4. *Tet2* deficiency preserves effector function and restricts terminal differentiation of CD8$^+$ TILs in CRC liver metastasis.**

(A) Nine subclusters were labeled with different colors on the UMAP plot of the total 2,202 CD8$^+$ TILs from both *Tet2*$^{fl/fl}$ group ($n$ = 2) and *Vav1*$^{Cre}$*Tet2KO* group ($n$ = 2).

(B) UMAP plot of CD8$^+$ TIL subclusters of each mouse group (1,101 CD8$^+$ TILs for each group). The pie plots show percentages of each CD8$^+$ TIL subcluster in each group.

(C) Bubble plot showing the expression of selected marker genes among the top 50 most significant DEGs across defined clusters. The list of the top 50 most significant DEGs for each cluster are provided in Table S16.

(D) Volcano plot displaying DEGs between *Tet2*$^{fl/fl}$ and *Vav1*$^{Cre}$*Tet2KO* CD8$^+$ TILs, highlighting T-cell exhaustion markers and cytolytic/effector-associated genes (adjusted $P$ value < 0.05). List of DEGs is provided in Table S17.

(E) Box plots comparing the enrichment scores of effector versus exhausted T-cell signatures ($p$ = 0.013) and memory versus exhausted T-cell signatures ($p$ < 0.0001) between *Tet2*$^{fl/fl}$ and *Vav1*$^{Cre}$*Tet2KO* CD8$^+$ TILs.

(F) Heatmap displaying the average expression of 42 exhaustion-associated marker genes across subclusters and genotypes.

(G) UMAP plot with cells labeled by exhaustion score characterize the spectrum of exhausted T cells with positive scoring values increasing toward $T_{TEX}$.

(H) Box plot comparing exhaustion scores between *Tet2*$^{fl/fl}$ and *Tet2KO* CD8$^+$ TILs ($p$ = 0.046).

(I) Pseudotime trajectory of CD8$^+$ TIL subclusters inferred by Monocle3 (left), with cells ordered along the trajectory using *Ly6c2*$^{low}$ $T_{SLC}$ as the root (right). Arrows indicate inferred differentiation paths toward $T_{EFF}$ and $T_{TEX}$ states.

(J) UMAP plot with cells colored by TCR clonal size categories, showing the distribution of clones across states in each group.

(K) TCR repertoire overlap analysis using the Morisita overlap index between progenitor-like, effector, and exhausted states across groups.

TILs, tumor-infiltrating lymphocytes; CRC, colorectal cancer; UMAP, Uniform Manifold Approximation and Projection; DEG, differentially expressed gene; $T_{TEX}$, terminally exhausted T cell; $T_{EFF}$, cytotoxic/effector-like exhausted T cells; $T_{SLC}$, stem-like CD8 T cell; TCR, T-cell receptor.

Statistical significance in (E) and (H) was determined by Mann-Whitney U test. *$p < 0.05$, **$p < 0.01$, ***$p < 0.001$, ****$p < 0.0001$, ns = not significant.

339 ***Tet2* deficiency cell-intrinsically restrains terminal exhaustion and enables sustained**
340 **effector generation via progenitor preservation**

341 To directly assess whether *Tet2* regulates T-cell exhaustion in a cell-intrinsic manner, we
342 utilized an *in vitro* chronic TCR stimulation model using purified CD8 T cells from
343 *Cd4*$^{Cre}$*Tet2KO* and *Tet2*$^{fl/fl}$ mice. Following initial activation with plate-bound anti-CD3ε and
344 soluble anti-CD28 antibodies, cells were repeatedly re-stimulated with anti-CD3ε antibody
345 alone to mimic persistent antigen exposure (Figure 5A).

346 Flow cytometric analysis at days 7 and 12 revealed that *Tet2* deficiency selectively
347 altered exhaustion fate decisions (Figures 5B and 5C). *Tet2KO* CD8 T cells displayed
348 significantly lower frequencies of PD-1$^{+}$Tim3$^{+}$T$_{TEX}$ and PD-1$^{+}$Tcf1$^{-}$T$_{TEX}$, accompanied by a
349 significant enrichment of PD-1$^{+}$Tcf1$^{+}$ PD-1$^{+}$ progenitor exhausted T (T$_{PEX}$) cells at both
350 timepoints (Figures 5B and 5C, Table S19A and S19B). Notably, longitudinal analysis
351 further demonstrated that *Tet2* is required for progressive depletion of the progenitor
352 exhausted compartment. Between days 7 and 12, the PD-1$^{+}$Tcf1$^{+}$T$_{PEX}$ pool was markedly
353 reduced in *Tet2*$^{fl/fl}$ cultures, whereas this population was maintained in *Tet2KO* CD8 T cells,
354 despite accelerated T$_{TEX}$-cell accumulation in both genotypes (Figure 5D; Table S19C).
355 These findings validate our scRNA-seq-based observations and establish *Tet2* as a cell-
356 intrinsic regulator that promotes terminal exhaustion commitment at the expense of the
357 progenitor population under chronic TCR stimulation.

358 We next examined how *Tet2* deficiency influences memory and effector
359 differentiation states during prolonged TCR signaling. Consistent with their exhaustion
360 profile, *Tet2*$^{fl/fl}$ CD8 T cells exhibited significantly higher proportions of CD44$^{+}$CD62L$^{-}$

361 effector/effector memory ($T_{EM/EFF}$) cells, whereas *Tet2KO* CD8 T cells retained significantly
362 higher frequencies of $CD44^{+}CD62L^{+}$ central memory-like ($T_{CM}$) cells at both days 7 and 12
363 (Figures 5E and 5F; Table S19A and S19B). Notably, although *Tet2KO* cells displayed lower
364 $T_{EM/EFF}$ proportions at individual timepoints, longitudinal analysis revealed robust
365 differentiation capacity. From day 7 to day 12, *Tet2KO* cultures exhibited a 6.69-fold
366 expansion of the $T_{EM/EFF}$ compartment, exceeding the 3.24-fold increase observed in *Tet2*$^{fl/fl}$
367 cells (Figures 5G and 5H). Importantly, enhanced effector output in *Tet2KO* cells was
368 achieved without excessive attrition of self-renewing populations. *Tet2KO* naive CD8 T cells
369 ($T_{NAIVE}$) were not significantly depleted over time, and while $T_{CM}$ frequencies declined in
370 both genotypes, *Tet2KO* cells exhibited lower fold reductions, indicating superior
371 preservation of self-renewing memory compartments (Figures 5G and 5H; Table S19C).
372 Together, these data demonstrate that *Tet2* deficiency decouples effector generation from
373 progenitor depletion, enabling sustained differentiation while preserving $Tcf1^{+}T_{PEX}$ and
374 $CD62L^{+}T_{CM}$-like reservoirs under chronic TCR stimulation.

375 Figure 5

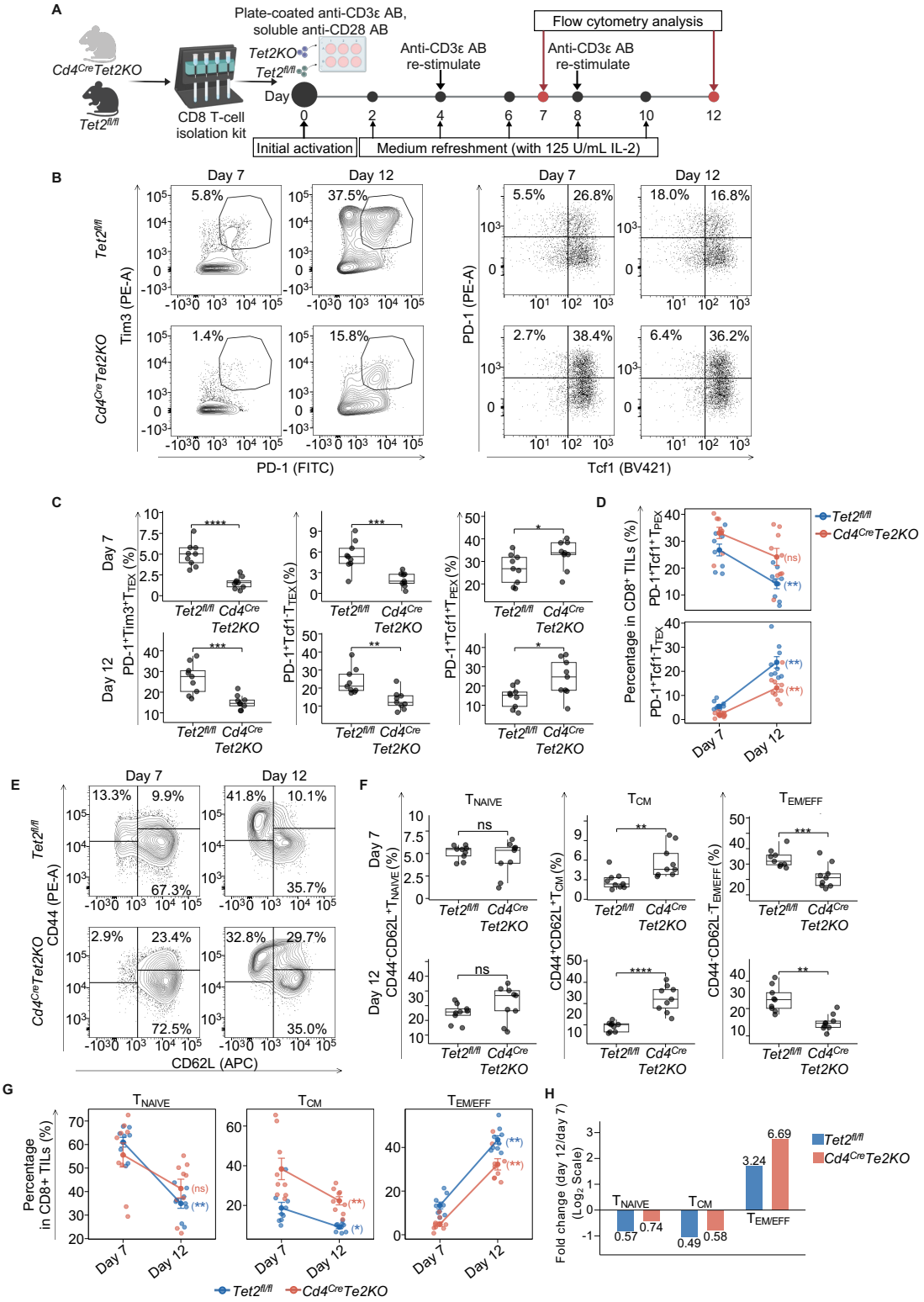
A
Plate-coated anti-CD3ε AB, soluble anti-CD28 AB
Flow cytometry analysis
Cd4CreTet2KO
Tet2fl/fl
Tet2KO
Anti-CD3ε AB re-stimulate
Anti-CD3ε AB re-stimulate
CD8 T-cell isolation kit
Day
0 2 4 6 7 8 10 12
Initial activation
Medium refreshment (with 125 U/mL IL-2)
B
Day 7
Day 12
Tim3 (PE-A)
PD-1 (FITC)
PD-1 (PE-A)
Tcf1 (BV421)
5.8%
37.5%
1.4%
15.8%
5.5%
26.8%
18.0%
16.8%
2.7%
38.4%
6.4%
36.2%
C
Day 7
Day 12
PD-1+Tim3+TTEX (%)
PD-1+Tcf1-TTEX (%)
PD-1+Tcf1+TPEX (%)
Tet2fl/fl
Cd4CreTet2KO
D
Percentage in CD8+ TILs (%)
PD-1+Tcf1+TPEX
PD-1+Tcf1-TTEX
Day 7
Day 12
E
Day 7
Day 12
CD44 (PE-A)
CD62L (APC)
13.3%
9.9%
67.3%
41.8%
10.1%
35.7%
2.9%
23.4%
72.5%
32.8%
29.7%
35.0%
F
TNAIVE
TCM
TEM/EFF
CD44+CD62L+TNAIVE (%)
CD44+CD62L+TCM (%)
CD44-CD62L-TEM/EFF (%)
ns
G
Percentage in CD8+ TILs (%)
H
Fold change (day 12/day 7) (Log2 Scale)
0.57
0.74
0.49
0.58
3.24
6.69

**Figure 5. *Tet2* deficiency cell-intrinsically restrains terminal exhaustion while preserving self-renewing progenitor pools under chronic TCR stimulation.**

(A) Experimental design for *in vitro* chronic TCR stimulation assay. CD8 T cells isolated from *Cd4*$^{Cre}$*Tet2KO* and *Tet2*$^{fl/fl}$ mice ($n$ = 9 per group) were activated with anti-CD3ε (2 μg/mL) and soluble anti-CD28 (2 μg/mL) antibodies, then chronically re-stimulated with anti-CD3ε antibody alone (2 μg/mL) on days 4 and 8 to model persistent antigen exposure. Cells were analyzed by flow cytometry at days 7 and 12.

(B) Representative flow cytometry plots showing expression of exhaustion markers PD-1 and Tim3 (left), and PD-1 and Tcf1 (right) at days 7 and 12 in *Tet2*$^{fl/fl}$ (top row) and *Tet2KO* (bottom row) CD8 T cells.

(C) Quantification of exhaustion phenotypes. Box plots comparing frequencies of PD-1$^{+}$Tim3$^{+}$$T_{TEX}$, PD-1$^{+}$Tcf1$^{-}$$T_{TEX}$, and PD-1$^{+}$Tcf1$^{+}$$T_{PEX}$ between *Tet2KO* and *Tet2*$^{fl/fl}$ groups at day 7 (top) and day 12 (bottom). See also Table S19A and S19B for detailed quantification and statistical comparisons.

(D) Temporal dynamics of exhaustion differentiation. Longitudinal plots showing longitudinal changes from day 7 to day 12 of PD-1$^{+}$Tcf1$^{+}$$T_{PEX}$ (top), and PD-1$^{+}$Tcf1$^{-}$$T_{TEX}$ (bottom). See also Table S19A and S19C for detailed quantification and statistical comparisons.

(E) Representative flow cytometry plots showing CD62L and CD44 expression patterns at days 7 and 12 in *Tet2*$^{fl/fl}$ (top row) and *Tet2KO* (bottom row) CD8 T cells.

(F) Quantification of memory and effector differentiation states. Box plots comparing frequencies of CD44$^{-}$CD62L$^{+}$$T_{NAIVE}$, CD44$^{+}$CD62L$^{+}$$T_{CM}$, and CD44$^{+}$CD62L$^{-}$$T_{EM/EFF}$ between *Tet2KO* and *Tet2*$^{fl/fl}$ groups at day 7 and day 12. See also Table S19A and S19B for detailed quantification and statistical comparisons.

(G) Temporal dynamics of $T_{NAIVE}$, $T_{CM}$, and $T_{EM/EFF}$ populations. Longitudinal plots show longitudinal changes from day 7 to day 12 of the indicated populations (left to right). See also Table S19A and Table S19C for detailed quantification and statistical comparisons.

(H) Fold changes (day 12/day 7) on log2 scale quantifying differentiation kinetics. Numbers on bars indicate actual fold change values; y-axis is log2-transformed to show proportional changes.

TCR, T-cell receptor; $T_{TEX}$, terminally exhausted T cells; $T_{PEX}$, progenitor exhausted T cells; $T_{CM}$, central memory T cells; $T_{EM/EFF}$, effector memory/ effector T cells; $T_{NAIVE}$, Naïve T cells; AB, antibody. Data in (C), (D), (F), and (G) are compiled from three independent experiments (total $n$ =

9 mice per group). Statistical significance for temporal comparisons (Day 7 vs. Day 12 within each genotype) determined by Wilcoxon signed-rank test (paired, two-tailed). Statistical significance for group comparisons (*Tet2*$^{fl/fl}$ vs. *Tet2KO* at each timepoint) determined by Mann-Whitney U test (unpaired, two-tailed). *$p < 0.05$, **$p < 0.01$, ***$p < 0.001$, ****$p < 0.0001$, ns = not significant.

377 ***Tet2* loss induces genome-wide hypermethylation and epigenetic silencing of the**
378 **exhaustion regulator *Tox* in PD-1$^+$CD8$^+$ TILs**

379 To determine whether *Tet2* loss impairs active DNA demethylation in CD8$^+$ TILs, we
380 performed whole genome bisulfite sequencing (WGBS) on activated PD-1$^+$CD8$^+$ TILs
381 isolated from liver metastatic tumors in *Vav1$^{Cre}$Tet2KO* and control *Tet2$^{fl/fl}$* mice (Figure 6A).
382 WGBS analysis comparing *Tet2KO* to *Tet2$^{fl/fl}$* PD-1$^+$CD8$^+$ TILs identified 19,492
383 differentially methylated regions (DMRs) across all chromosomes, of which 98.8% were
384 hypermethylated in *Tet2KO* cells (Figures S8A-C). Among these, 5,751 DMRs were mapped
385 to annotated genomic loci corresponding to 4,260 genes (Figure S8D; Table S20). A total of
386 2,644 DMRs were located in regulatory elements, including enhancer, promoter,
387 transcription start site (TSS), or CTCF-binding regions, and were designated as regulatory
388 DMRs (rDMRs) (Figure 6B; Table S21). In addition, the majority of rDMRs were distributed
389 within the enhancer or promoter regions (Figure 6B). Notably, *Tet2KO* PD-1$^+$CD8$^+$ TILs
390 exhibited a marked predominance of hypermethylated rDMRs (hyper-rDMRs; $n$ = 2,519)
391 compared with hypomethylated rDMRs (hypo-rDMRs; $n$ = 125) (Figure 6C). Integration of
392 WGBS with scRNA-seq revealed 22 genes with predominantly hypermethylated rDMRs that
393 were also transcriptionally downregulated in *Tet2KO* PD-1$^+$CD8$^+$ TILs compared to *Tet2$^{fl/fl}$*
394 PD-1$^+$CD8$^+$ TILs (Figures 6D; Table S22). Among these, *Tox*, a master regulator of T-cell
395 exhaustion, showed one of the most extensive methylation changes genome-wide (Figures
396 6D and S8E). A methylation impact score (total DMR count × mean absolute methylation
397 difference) (see Methods) similarly ranked *Tox* second and highlighted its widespread
398 hypermethylation across multiple regulatory regions (Figure S8F).

399 Within the *Tox* locus, differentially methylated CpG site (DMC) analysis identified
400 89 DMCs among 735 CpGs, all showing increased methylation in *Tet2KO* PD-1$^{+}$CD8$^{+}$ TILs
401 relative to *Tet2*$^{fl/fl}$ PD-1$^{+}$CD8$^{+}$ TILs, with a mean gain of 58.2% (Figures 6E, 6F and S8G-
402 S8I; Table S23). DMR analysis focusing on the *Tox* locus using 500bp-window screening
403 revealed 56 significant DMRs with a mean methylation increase of 47.2% (Figures 6G and
404 S8J; Table S24). Notably, *Tox* showed extensive hypermethylation at regulatory elements,
405 including 8 enhancer DMRs with mean methylation difference of 45.2%, and 4 CTCF
406 binding site DMRs with mean methylation difference of 49.3% (Figures 6G and 6H). These
407 findings indicate that *Tet2* deficiency induces broad hypermethylation at critical regulatory
408 elements of *Tox*, leading to transcriptional repression of this central exhaustion-program
409 regulator in *Tet2KO* PD-1$^{+}$CD8$^{+}$ TILs.

410 Figure 6

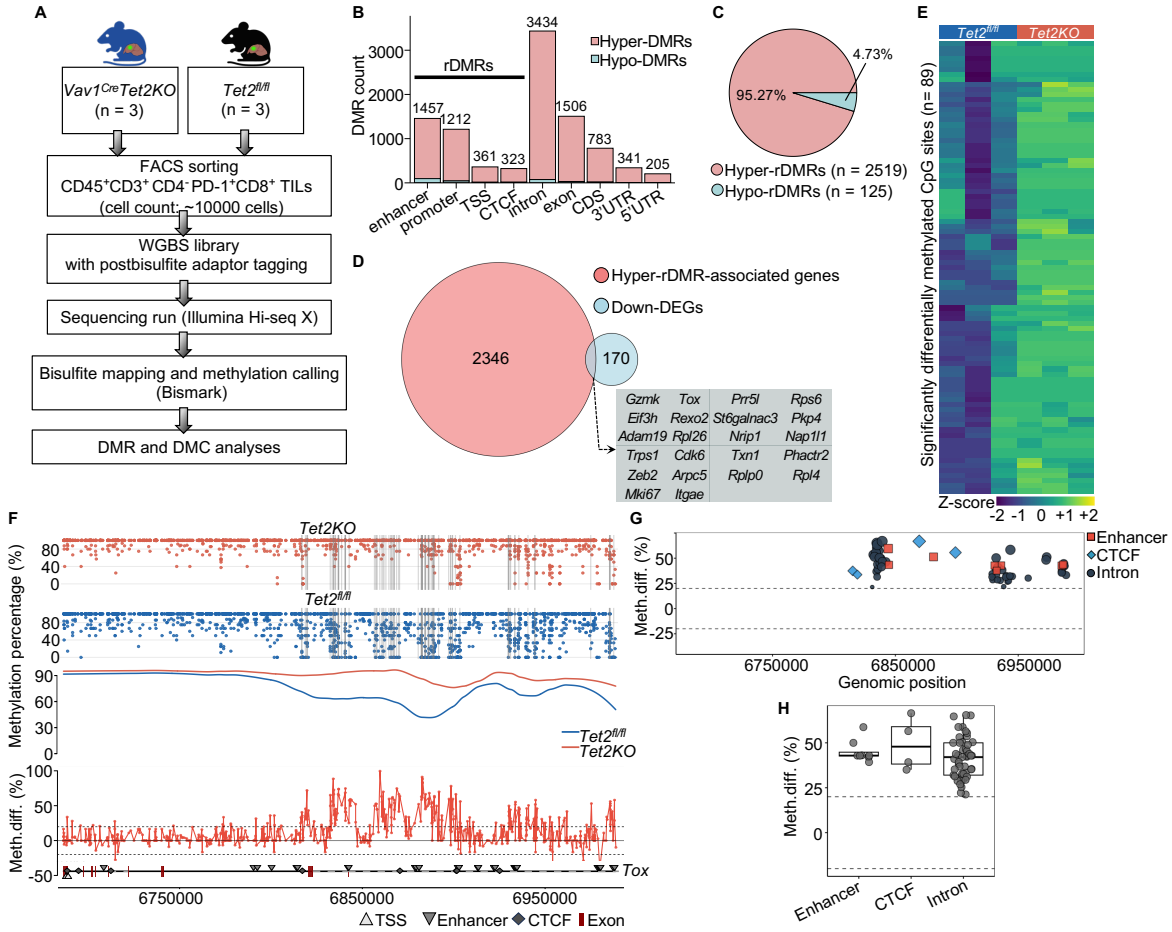
A
Vav1CreTet2KO (n = 3)
Tet2fl/fl (n = 3)
FACS sorting
CD45+CD3+ CD4- PD-1+CD8+ TILs
(cell count: ~10000 cells)
WGBS library
with postbisulfite adaptor tagging
Sequencing run (Illumina Hi-seq X)
Bisulfite mapping and methylation calling
(Bismark)
DMR and DMC analyses
B
DMR count
rDMRs
Hyper-DMRs
Hypo-DMRs
1457
1212
361
323
3434
1506
783
341
205
enhancer
promoter
TSS
CTCF
intron
exon
CDS
3'UTR
5'UTR
C
4.73%
95.27%
Hyper-rDMRs (n = 2519)
Hypo-rDMRs (n = 125)
D
Hyper-rDMR-associated genes
Down-DEGs
2346
170
Gzmk Tox Prr5l Rps6
Eif3h Rexo2 St6galnac3 Pkp4
Adam19 Rpl26 Nrip1 Nap1l1
Trps1 Cdk6 Txn1 Phactr2
Zeb2 Arpc5 Rplp0 Rpl4
Mki67 Itgae
E
Tet2fl/fl
Tet2KO
Significantly differentially methylated CpG sites (n= 89)
Z-score
-2 -1 0 +1 +2
F
Tet2KO
Tet2fl/fl
Methylation percentage (%)
Meth.diff. (%)
Tox
6750000
6850000
6950000
TSS
Enhancer
CTCF
Exon
G
Meth.diff. (%)
Enhancer
CTCF
Intron
6750000
6850000
6950000
Genomic position
H
Meth.diff. (%)
Enhancer
CTCF
Intron

**Figure 6. *Tet2* loss induces genome-wide hypermethylation and epigenetic silencing of *Tox* in PD-1$^+$CD8$^+$ TILs.**

(A) Schematic overview of WGBS workflow for analyzing DNA methylation in PD-1$^+$CD8$^+$ TILs.

(B) Distribution of DMRs across genomic features in *Tet2KO* vs. *Tet2$^{fl/fl}$* PD-1$^+$CD8$^+$ TILs. DMRs located at enhancer, promoter, TSS, or CTCF-binding regions, and were designated as regulatory DMRs (rDMRs).

(C) Pie chart displaying the proportion of hyper-rDMRs ($n$ = 2519, 95.3%) versus hypo-rDMRs ($n$ = 125, 4.7%).

(D) Venn diagram identifying 22 genes showing coordinated hypermethylation ($q$-value < 0.01, meth.diff > 0.2) and transcriptional downregulation (min.pct = 0.1, adjusted $P$ value < 0.05) in *Tet2KO* PD-1$^+$CD8$^+$ TILs, including the master exhaustion regulator *Tox*.

(E) Heatmap displaying 89 significant DMCs across the *Tox* locus identified by DMC analysis, with Z-scores indicating methylation levels in *Tet2$^{fl/fl}$* and *Tet2KO* replications.

(F) Genome browser view of the *Tox* locus at CpG resolution showing methylation percentage at 735 CpG sites in *Tet2$^{fl/fl}$* (blue) and *Tet2KO* (red) PD-1$^+$CD8$^+$ TILs, with smoothed methylation trends and methylation difference plot below, the grey bars highlighting 89 significant DMCs. Gene structure indicates TSS, enhancers, CTCF binding sites, and exons.

(G) Scatter plot of methylation percentage differences across the *Tox* gene structure by DMR analysis, displaying 56 rDMRs at enhancer, CTCF, and intronic regions.

(H) Box plots of methylation percentage differences at enhancer, CTCF, and intronic regions within the *Tox* locus.

TIL, tumor-infiltrating lymphocytes; WGBS, whole genome bisulfite sequencing; DMR, differentially methylated region; DMC, differentially methylated cytosine; TSS, transcription start site; CTCF, CCCTC-binding factor; CDS, coding sequence; UTR, untranslated region; min.pct, minimum percentage of cells. For (B)-(H), statistical significance to identify DMRs and DMCs determined by *methylKit* using $q$-value < 0.01 and |meth.diff| ≥ 20%.

411

412 ***Tet2KO:Tet2WT* chimeric mouse model of CH demonstrates restricted tumor growth**
413 **and intrinsic resistance of *Tet2*-deficient CD8$^+$ TILs to terminal exhaustion**
414 To model the mosaicism of tumor-infiltrating immune cells observed in solid tumor patients
415 with CH, in which mutant and wild-type hematopoietic cells coexist within the tumor
416 microenvironment, we established a competitive bone marrow transplantation (BMT) mouse
417 model of CRC liver metastasis (Figure 7A). Lethally irradiated CD45.1$^+$ wild-type (WT)
418 recipients were reconstituted with mixtures of *Vav1*$^{Cre+}$*Tet2*$^{fl/fl}$ CD45.2$^+$ BM cells and *Tet2WT*
419 CD45.1$^+$/CD45.2$^+$ competitor BM cells at ratios of 1:2 or 1:3, generating *Tet2KO:Tet2WT*
420 mixed chimeras. Control *Tet2*$^{fl/fl}$*:Tet2WT* chimeras received a 1:1 mixture of *Tet2*$^{fl/fl}$ CD45.2$^+$
421 and *Tet2WT* CD45.1$^+$/CD45.2$^+$ BM cells. Four weeks post-BMT, flow cytometric analysis of
422 peripheral blood confirmed successful hematopoietic reconstitution, with donor-derived
423 CD45.2$^+$ cells constituting >95% of B220$^+$ B lymphocytes, CD11b$^+$ myeloid cells, and
424 NK1.1$^+$ natural killer cells (Figure S9A). As expected from radio-resistant host T cell
425 survival[48], approximately 25.9 ± 1.8% recipient-derived CD45.1$^+$ T cells remained within the
426 CD3$^+$ T cell population (Figure S9A). Subsequently, Venus-*AKTP*$^{M/LOH}$ CRC cells were
427 injected intrasplenically to induce liver metastases in these reconstituted chimeric mice
428 (Figure 7A).
429 Twelve weeks post-BMT, *Tet2KO* cells exhibited progressive competitive expansion
430 relative to *Tet2WT* cells across all immune cell subsets compared with the four-week post-
431 BMT baseline, with the most pronounced expansion in myeloid cell populations (Figure S9B;
432 Table S25A and S25B). In contrast, control chimeras showed no competitive advantage of
433 *Tet2*$^{fl/fl}$ cells over *Tet2WT* competitor cells, maintaining stable ratios throughout the

434 observation period (Figure S9B; Table S25A and S25B). This clonal expansion pattern
435 recapitulates the progressive outgrowth of somatic *TET2* mutant-derived CH observed in
436 human patients[49]. Within liver metastases of *Tet2KO:Tet2WT* chimeras, *Tet2KO* T cells
437 accounted for approximately 35–46% of total T cells and 23–32% of the $CD8^+$ TIL subset.
438 These frequencies were comparable to the $Tet2^{fl/fl}$ $CD45.2^+$ populations observed in controls
439 (Figure S9C; Table S25C).

440 Consistent with the restricted LMTB observed in $Vav1^{Cre}/Cd4^{Cre}Tet2KO$ mice,
441 *Tet2KO:Tet2WT* chimeric mice demonstrated significantly reduced LMTB compared to
442 $Tet2^{fl/fl}$*:Tet2WT* controls (Figures 7B and S9D). Flow cytometric analysis of liver TILs
443 revealed a markedly higher proportion of $PD\text{-}1^+Tim3^+$ $T_{TEX}$ in both $Tet2^{fl/fl}$ $CD45.2^+$ and
444 residual recipient *Tet2WT* $CD45.1^+$ populations compared to that in *Tet2KO* $CD45.2^+$ $CD8^+$
445 TILs (Figures 7C and 7D; Table S25D). Collectively, these data demonstrate that even within
446 a competitive environment containing *Tet2WT* counterparts, *Tet2*-deficient $CD8^+$ TILs
447 exhibit an intrinsic resistance to terminal exhaustion.

448 Figure 7

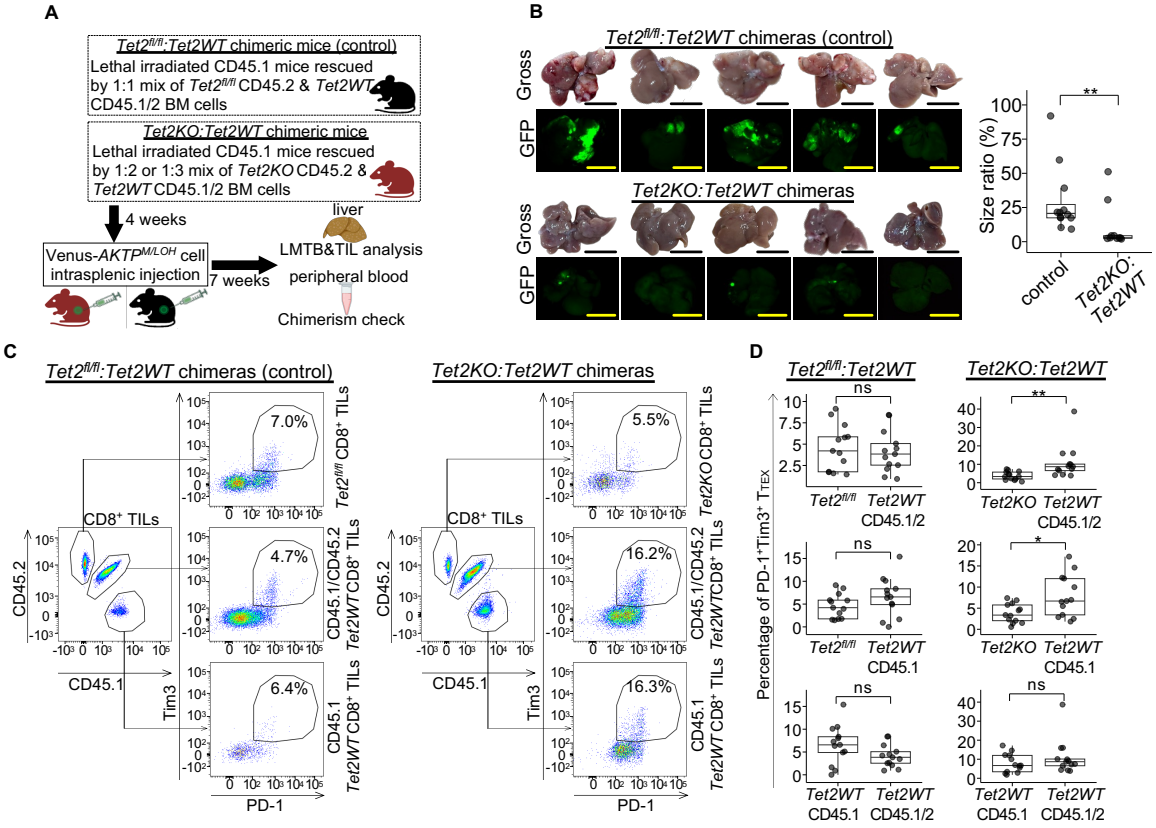
A
Tet2fl/fl:Tet2WT chimeric mice (control)
Lethal irradiated CD45.1 mice rescued by 1:1 mix of Tet2fl/fl CD45.2 & Tet2WT CD45.1/2 BM cells
Tet2KO:Tet2WT chimeric mice
Lethal irradiated CD45.1 mice rescued by 1:2 or 1:3 mix of Tet2KO CD45.2 & Tet2WT CD45.1/2 BM cells
4 weeks
Venus-AKTPM/LOH cell intrasplenic injection
7 weeks
liver
LMTB&TIL analysis
peripheral blood
Chimerism check
B
Tet2fl/fl:Tet2WT chimeras (control)
Gross
GFP
Tet2KO:Tet2WT chimeras
Size ratio (%)
control
Tet2KO:Tet2WT
C
Tet2fl/fl:Tet2WT chimeras (control)
Tet2KO:Tet2WT chimeras
CD8+ TILs
CD45.2
CD45.1
Tim3
PD-1
7.0%
4.7%
6.4%
5.5%
16.2%
16.3%
Tet2fl/fl CD8+ TILs
Tet2WT CD8+ TILs
Tet2KO CD8+ TILs
CD45.1/CD45.2
D
Tet2fl/fl:Tet2WT
Tet2KO:Tet2WT
Percentage of PD-1+Tim3+ TTEX
ns
Tet2fl/fl
Tet2WT
CD45.1/2
Tet2KO
CD45.1

**Figure 7** ***Tet2KO:Tet2WT*** **chimeric mouse model of CH demonstrates restricted tumor growth and intrinsic resistance of** ***Tet2*****-deficient CD8$^+$ TILs to terminal exhaustion in CRC liver metastasis.**

(A) Experiment schema of *Tet2KO:Tet2WT* chimeric mouse model with CRC liver metastasis. Lethally irradiated CD45.1$^+$ WT-recipients were reconstituted with mixtures of *Vav1$^{Cre+}$Tet2$^{fl/fl}$* CD45.2$^+$ and *Tet2WT* CD45.1$^+$/CD45.2$^+$ BM cells at ratios of 1:2 or 1:3 (KO : WT competitor) to generate *Tet2KO:Tet2WT* mixed chimeras. Control *Tet2$^{fl/fl}$*:*Tet2WT* chimeras received a 1:1 mixture of *Tet2$^{fl/fl}$* CD45.2$^+$ and *Tet2WT* CD45.1$^+$/CD45.2$^+$ BM cells. Four weeks post-transplantation, Venus-*AKTP$^{M/LOH}$* colorectal cancer cells were intrasplenically injected. Chimerism was assessed in peripheral blood 8 weeks post-injection, followed by analysis of CD8$^+$ TILs and LMTB.

(B) Representative liver metastasis samples and box plot comparing LMTB between *Tet2KO:Tet2WT* chimeric mice ($n$ = 10) and *Tet2$^{fl/fl}$*:*Tet2WT* controls ($n$ = 12) (29.1 ± 24.1% vs. 10.6 ± 16.7%; $p$ = 0.0076). Scale bars: 1 cm.

(C) Representative flow cytometry plots showing the proportion of PD-1$^+$Tim3$^+$ CD8 $T_{TEX}$ in *Tet2$^{fl/fl}$* CD45.2$^+$, host-derived *Tet2WT* CD45.1$^+$, and *Tet2KO* CD45.2$^+$ CD8$^+$ TILs.

(D) Box plots comparing frequencies of PD-1$^+$Tim3$^+$ CD8 $T_{TEX}$ across donor and host CD8$^+$ TIL populations ($n$ = 13 per group). See also Table S25D for detailed quantification and statistical comparisons.

CH, clonal hematopoiesis; TILs, tumor-infiltrating lymphocytes; CRC, colorectal cancer; BM, bone marrow; LMTB, liver metastatic tumor burden; $T_{TEX}$, terminally exhausted T cells. Data in (B) and (D) are compiled of at least 2 independent experiments and presented as mean ± SD. Statistical significance was determined by Mann-Whitney U test. *$p$ < 0.05, **$p$ < 0.01, ***$p$ < 0.001, ****$p$ < 0.0001, ns = not significant.

449

450 ***Anti-PD-1 treatment suppresses CRC liver metastasis in Tet2$^{fl/fl}$ mice***

451 Given the enrichment of exhaustion markers in *Tet2$^{fl/fl}$* CD8$^{+}$ TILs, we evaluated the
452 therapeutic efficacy of PD-1 blockade (Figure S10A). *Tet2$^{fl/fl}$* mice treated with anti-PD-1
453 antibody exhibited complete tumor eradication, whereas IgG-treated controls developed
454 profound liver metastatic growth (Figures S10B and S10C). Although IgG-treated
455 *Vav1$^{Cre}$Tet2KO* mice displayed reduced LMTB compared to *Tet2$^{fl/fl}$* controls (IgG-treated
456 *Vav1$^{Cre}$Tet2KO* vs. IgG-treated *Tet2$^{fl/fl,}$* 0.54 ± 0.39 mm2 vs. 23.53 ± 12.64 mm2, $p$ = 0.008),
457 minimal residual tumors persisted (Figures S10B and S10C). This indicates that targeting the
458 PD-1 axis is sufficient to reverse the metastasis-permissive environment associated with
459 *Tet2*-intact hematopoiesis.

460

461 **DISCUSSION**

462 While CH is highly prevalent among patients with solid tumors, its impact on fundamental
463 aspects of cancer biology, including tumor growth, treatment response, and metastasis, has
464 remained poorly defined[21,26,50,51]. In this study, we demonstrate that *TET2*-mutant CH confers
465 protection against cancer metastasis, extending prior observations that *TET2* inactivation can
466 enhance anti-tumor immunity in settings such as chimeric antigen receptor T-cell therapy[52,53]
467 and immune checkpoint blockade[15,33]. By integrating large-scale clinical data with genetic
468 and functional mouse models, we identify *TET2*-mutant CH as a previously unrecognized
469 tumor-suppressive state that limits metastatic outgrowth.

470 In a cohort of over 16,000 solid tumor patients, we show that individuals with *TET2*-
471 driver clonal hematopoiesis have significantly lower odds of presenting with metastatic

472 disease and exhibit reduced metastatic burden. Notably, although *TET2*-mutant CH is
473 generally considered an adverse condition due to its association with increased morbidity and
474 mortality from atherosclerotic and fibrotic diseases[54-57], we did not observe a difference in
475 median survival between solid tumor patients without CH and those with *TET2*-CH. This
476 finding stands in contrast to patients harboring CH driven by mutations in DNA damage
477 response, cohesin, or spliceosome genes, who experienced significantly worse overall
478 survival, consistent with prior studies[22,23,27,58]. Together, these data suggest that the biological
479 consequences of CH are highly driver dependent, and that *TET2*-mutant CH differs
480 fundamentally from other high-risk CH genotypes in the context of solid tumor
481 microenvironments.

482 Our liver metastasis models provide functional evidence supporting a causal
483 relationship between *TET2*-mutant CH and protection from metastatic disease. Both
484 complete and chimeric pan-hematopoietic *Tet2* inactivation were sufficient to attenuate
485 metastatic outgrowth, demonstrating that this association is not merely correlative.
486 Importantly, we show that *Tet2*-deficient CD8 T cells are necessary and sufficient for the
487 anti-metastatic effect of *TET2*-mutant CH, linking this phenotype directly to adaptive
488 immune function. This finding helps reconcile prior heterogeneous reports on the impact of
489 *Tet2*-mutant CH in syngeneic tumor models, where tumor growth has been reported as
490 promoted, suppressed, or unaffected depending on tumor type, implantation site, and
491 experimental context[29,30,59]. Indeed, our patient-level analyses revealed tumor-type–specific
492 variation, with the strongest protective association observed for liver and brain metastasis.

493 Mechanistically, our data established that *Tet2* deficiency restrains metastatic
494 progression by limiting terminal CD8 T cell exhaustion. Tet2 is transcriptionally induced
495 following T cell receptor engagement[53,60] and has been shown to act as a negative regulator
496 of adaptive immunity by catalyzing DNA demethylation at key regulatory loci, thereby
497 favoring differentiation toward exhausted or regulatory states at the expense of durable
498 memory[60,61]. In the context of CH, this negative feedback is diminished. Within metastatic
499 liver lesions, *Tet2*-deficient $CD8^+$ TILs exhibit sustained methylation at regulatory elements
500 of the *Tox* locus, resulting in transcriptional repression of TOX, a master regulator of terminal
501 exhaustion[62,63]. This epigenetic constraint preserves progenitor and stem-like CD8 T cell
502 states and enables sustained effector generation under chronic antigen stimulation.

503 These findings define a TET2–DNA methylation–TOX axis as a central epigenetic
504 checkpoint governing exhaustion fate commitment in CD8 T cells. Similar mechanisms have
505 been implicated in enhanced control of chronic infection and cancer by *Tet2*-mutant CD8 T
506 cells and *Tet2*-deficient CAR-T cells[53], underscoring the generalizability of this regulatory
507 pathway. However, unrestrained T-cell activation associated with *TET2*-mutant CH may also
508 be pathological in certain contexts, including autoimmunity[64,65], immune-related toxicities
509 during immunotherapy[66], or malignant transformation following acquisition of additional
510 mutations[67,68]. Indeed, *TET2*-mutant CH is a recognized risk factor for T cell lymphoma[69] ,
511 highlighting the dual-edged nature of sustained immune activation.

512 In addition to its effects on T cells, *Tet2* loss has been shown to enhance antigen-
513 presenting capacity in macrophages[15]. While myeloid-restricted *Tet2* inactivation was
514 insufficient to suppress liver metastasis in our models, it may still contribute to improved

515 tumor control in concert with CD8 T cells. Consistent with this notion, we and others have
516 previously observed transcriptional signatures of heightened T-cell activation in colorectal
517 cancer and melanoma samples from patients with *TET2*-mutant CH[15,70]. Defining the relative
518 contributions of distinct immune lineages to other CH-associated clinical phenotypes remains
519 an important area for future investigation.

520 Several limitations of this study should be acknowledged. We were unable to directly
521 assess whether tumor-infiltrating *TET2*-mutant T lymphocytes correlate with metastatic
522 status in patients, as such data were not available. Although *TET2* is a well-established
523 negative regulator of CD8 T cell activity[53,60,71], the frequency and functional relevance of
524 *TET2*-mutant CD8 T cells within human tumors remain incompletely characterized.
525 Moreover, our experimental models focused on experimental liver metastasis and therefore
526 do not address potential effects of *TET2*-mutant CH on primary tumor growth, metastatic
527 dissemination, or circulation through blood and lymphatic compartments. While the *Cd4Cre*
528 model demonstrates that T cells are necessary and sufficient for the observed phenotype, the
529 potential contribution of other *Tet2*-deficient immune cells warrants further study. Finally,
530 the causes of death in solid tumor patients with high-risk CH are not known and may be
531 unrelated to metastatic disease.

532 In summary, we show that *TET2*-mutant CH suppresses cancer metastasis in both
533 patients and animal models by enforcing an epigenetic barrier to terminal CD8 T-cell
534 exhaustion. These findings reposition *TET2*-mutant CH as a protective modifier of tumor
535 progression and suggest that CH status may have utility as a prognostic biomarker for
536 metastatic risk, at least in certain cancers. Notably, the magnitude of metastatic suppression

537 conferred by *TET2*-mutant CH was substantial in our experimental models, approaching the
538 level of tumor control observed with immune checkpoint blockade, suggesting that
539 pharmacologic strategies designed to mimic hematopoietic *TET2* inactivation—or to target
540 downstream components of the TET2–TOX axis—could represent novel therapeutic
541 approaches for the prevention or treatment of metastatic disease.

542

543 **METHODS**

544 **Experimental model and subject details**

545 **Human study cohort**

546 Patients who were tested for clonal hematopoiesis using an MSK-IMPACT targeted
547 sequencing panel with somatic mutations from peripheral blood sequencing results curated
548 as putative drivers or non-drivers of CH in the Bolton *et al*. 2020 cohort who were also
549 evaluated for metastatic disease by Nyugen *et al*. 2022 were included in our sub-cohort
550 analysis. Study data containing anonymous patient identifiers were downloaded from
551 cBioPortal on September 4$^{th}$, 2025. Using variants reported by Bolton *et al.* 2020, clonal
552 hematopoiesis (CH) was called as a putative driver mutation with variant allele fraction
553 (VAF) $\geq$ 2%. Each mutation was defined as either putative (PD) or non-putative based on its
554 role in cancer pathogenesis and recurrence in an MSKCC in-house dataset of myeloid
555 neoplasms as in Bolton *et al.* 2020. It was further was defined as either a non-myeloid PD or
556 myeloid PD based on relevance to myeloid neoplasms specifically.

557

558 **Mice**

559 *Vav1*$^{Cre36}$, *Cd4*$^{Cre37}$, *Cd19*$^{Cre38}$, and *LysM*$^{Cre39}$ transgenic mice were crossed with *Tet2*$^{fl/fl}$
560 mice[35] to generate homozygous *Tet2*-knockout mice (*Vav1*$^{Cre}$*Tet2KO, Cd4*$^{Cre}$*Tet2KO*, and
561 *LysM*$^{Cre}$*Tet2KO*). *Tet2*$^{fl/fl}$ mice served as *Tet2* wild-type control. All mice were maintained in
562 a specific pathogen-free animal facility in the Laboratory of Animal Center, University of
563 Tsukuba. All animal procedures adhered to the The Regulations for Animal Experiments in
564 University of Tsukuba. Mouse genotyping was performed using genomic DNA extracted
565 either from tails by KAPA kit method (KAPA Biosystems) or from blood by QIAamp DNA
566 Blood Mini Kit (Qiagen). The primers used for genotyping are listed in Table S26.
567
568 **Organoid cell line**
569 Venus-labeled mouse intestinal tumor-derived organoid-originated cells simultaneously
570 carrying *Apc*$^{\Delta 716}$, *Kras*$^{+/G12D}$, *Tgfbr2*$^{-/-}$, and *Trp53*$^{R270H/LOH}$ mutations (Venus-
571 *AKTP*$^{M/LOH}$ cells) were established as previously described[40]. Venus-*AKTP*$^{M/LOH}$ cells were
572 cultured in Advanced DMEM/F-12 medium (Gibco, #2508872) supplemented with 10%
573 Fetal Bovine Serum (FBS, Hyclone, #AE25787263), 1% Penicillin-Streptomycin (PS,
574 Fujifilm, #168-23191), 0.3 μg/ml Rock inhibitor (Y27632, Fujifilm, #235-00513), 0.9 μg/ml
575 GSK-3 inhibitor (CHIR99021, R&D system, #4423), and 21 μg/ml ALK inhibitor (A8301,
576 R&D systems, #5640). For the passage, Venus-*AKTP*$^{M/LOH}$ cells were enzymatically
577 dissociated with 0.25% Trypsin at 37$^{o}$C for 10 minutes and mechanically dissociated by
578 pipetting.
579
580 **Method details**

581 **Clinical cohort data processing and statistical analysis**

582 (1) Clonal hematopoiesis mutation grouping

583 Patients were categorized as having CH if they had a variant annotated as CH PD in Bolton
584 *et al.* 2020[22]. Patients were then categorized as having a *TET2* or *DNMT3A* PD only if they
585 had no other CH-defining PD variants. Using a mutually exclusive hierarchical system,
586 patients were first categorized as having a *TET2* driver, followed by a *DNMT3A*, cohesin
587 (*STAG2, RAD21, SMC1, SMC3, PDS5A, PDS5B*), spliceosome (*SF3B1, SRSF2, ZRSR2,*
588 *U2AF1*), or DNA-damage-response driver (*PPM1D, CHEK2, TP53, ATM*). For example, if
589 a patient had both a cohesin (e.g. *STAG2*) and spliceosome (*SF3B1*) PD variant, they would
590 be categorized in the cohesin group. A patient with a *TET2* and *STAG2* PD variant would
591 also be categorized in the cohesin group.

592 (2) Quantification of cancer metastatic burden

593 Patients were labelled as metastatic patient or non-metastatic patient by Nguyen *et al*.. For
594 each patient with metastatic disease, the number of metastases and metastatic sites was
595 quantified. Patients were assigned as positive or negative for cancer metastases to various
596 organs including lung, liver, draining lymph node (DLN), brain, and bone.

597 (3) Clinical cohort statistical analysis

598 The odds of metastatic disease stratified by each PD variant group was assessed using
599 multivariate logistic models to account for covariates that have previously been linked either
600 to CH prevalence or cancer outcome, including chemotherapy and radiation treatment status,
601 age, sex, smoking status, race, and cancer type. Similar models were used to assess odds of
602 metastasis within cancer types for *TET2*-driver CH. However, due to few occurrences of non-

603 metastatic cancer in *TET2*-driver CRC patients and prostate cancer patients and limitations
604 of multivariate analysis, Fisher's exact test for count data was applied in addition to the
605 logistic model to ensure robust statistical testing. (Table S1). For odds of metastasis to
606 specific sites, one model for each metastatic site allowed for patients with metastases at
607 multiple sites (such as brain and bone) to be classified as positive for all metastatic sites.

608 To assess metastatic burden, Wilcoxon rank-sum tests were used to quantify
609 differences in distribution of both number of metastases, and number of metastatic sites.
610 Further, multivariate negative binomial generalized linear models were used to account for
611 the same covariates as above.

612 Patients were categorized in a mutually exclusive manner according to the criteria
613 outlined above to investigate associations between PD variant groups and survival. Kaplan-
614 Meier survival curves and a corresponding Cox proportional hazards model were used to
615 account for covariates previously linked to survival, including age, sex, race, cancer type,
616 smoking status, chemotherapy and radiation treatment status, and metastatic status.

617 Difference in distribution of age between CH driver patients and non-CH driver
618 patients was quantified using a multivariate linear model to account for covariates associated
619 with age, including age, sex, race, cancer type, smoking status, chemotherapy and radiation
620 treatment status, and metastatic status. The association between *ASXL1* CH driver mutation
621 prevalence and smoking status was assessed using a multivariate logistic model, as were the
622 associations between DNA-damage-response CH driver mutation prevalence with treatment
623 status, and metastatic disease with treatment status. Odds of metastatic disease in patients

624 with a *TET2* CH driver mutation as opposed to a *TET2* CH non-driver mutation was also
625 assessed using a multivariate logistic model.
626 All statistical tests are two-tailed, and analyses in which multiple comparisons were
627 made were corrected for multiple hypothesis testing in a false discovery rate (FDR)
628 controlled fashion. An FDR-controlled *P* value threshold of 0.05 was used to denote
629 significance.
630
631 **Venus-AKTP$^{M/LOH}$ cell injection, liver metastasis tumor burden (LMTB) evaluation**
632 Venus-*AKTP$^{M/LOH}$* cells were used for the mouse spleen injection after at least four times of
633 passage. One million ($1x10^6$) of thoroughly dissociated Venus-*AKTP$^{M/LOH}$* cells resolved in
634 30 µl of Matrigel Matrix (Corning) were injected into mouse spleen. Mouse livers were
635 harvested 30 days post-injection and imaged as whole organs using the fluorescence stereo
636 microscope equipped with the digital color microscope camera (M165 FC/DFC450C, Leica
637 Microsystems) at 4.6x magnification to macroscopically assess the presence of Venus-
638 *AKTP$^{M/LOH}$* cell metastasis. LMTB was evaluated as previously described[72]. Briefly,
639 formalin-fixed paraffin-embedded liver sections were stained with hematoxylin and eosin
640 (H&E). The tumor burden was quantified by calculating the ratio of the total tumor area to
641 the total liver section area using a Keyence BZ-X710 microscope and BZ-X analyzer
642 software The two-tailed Mann-Whitney U test with $\alpha = 0.05$ was used to compare the size
643 ratio between the two groups.
644
645 **Antibody-based depletion of CD8 T cells**

646 Anti-CD8α antibody treatment was initiated two days prior to intrasplenic injection of Venus-
647 *AKTP*$^{M/LOH}$ cells. InVivoMAb anti-mouse CD8α antibody (clone 2.43, BioXCell, #BE0061)
648 was diluted with Phosphate-Buffered Saline (PBS) to the concentration of 1μg/μL and
649 intraperitoneally injected at an initial dose of 200 μg/mouse, followed by 6 booster injections
650 of 100 μg/mouse every 4 days throughout the tumor progression course. Control mice
651 received PBS in volumes matching those used in the anti-CD8α antibody treatment schedule.
652 Mice were sacrificed 30 days after the injection of Venus-*AKTP*$^{M/LOH}$ cells to collect the
653 whole liver for LMTB evaluation.
654
655 **Enzymatic digestion of liver metastases and isolation of tumor-infiltrating immune cells**
656 **for flow cytometry**
657 Mouse livers were harvested 30 days post-injection. Liver metastatic tumors and surrounding
658 liver tissues 0.5 cm from the edge of tumors were minced into small pieces < 1mm$^3$. The
659 minced tumor tissue was then digested by 15 ml of digestion buffer containing 0.75 mg/ml
660 collagenase A (Sigma-Aldrich, #10103578001) and 50 μg/ml DNase I (Worthington
661 Biochemical, #LS002139) in DMEM (Gibco, #10567-014), and incubated at 37 °C with
662 shaking at 170 rpm for 30 mins. After tissue digestion, the cell suspension was first filtered
663 through a 70-μm cell strainer (Falcon) to remove larger debris. The resulting homogenate
664 was then further filtered through a 30-μm cell strainer (Miltenyi Biotec) to obtain a single-
665 cell suspension. Any remaining undigested lumps were further dissociated by gentle pipetting.
666 DMEM supplemented with 10% FBS (Hyclone, #AE25787263) and 1% Penicillin-
667 Streptomycin (PS, Fujifilm, #168-23191) was added to terminate the digestion. The cell

668 suspension was centrifuged at 163× *g* for 7 mins at 4 °C, and then the cell pellet was
669 resuspended in 5 ml of 40% Percoll (Cytiva, #17089102) in PBS. The cell suspension was
670 then slowly and carefully dropped on top of 3 ml of Histopaque-1083 (Sigma-Aldrich,
671 #10831) without mixing and centrifuged at 1000× *g* for 20 mins in brake off mode. The cells
672 concentrated at the interface layer were carefully aspirated and added into 30 ml of FACS
673 buffer (PBS containing 2% Bovine Serum Albumin (BSA) and 2 mM EDTA) and centrifuged
674 at 800× *g* for 5 mins at 4 °C. To detect
675 exhausted T cells, the yielded cell pellet was resuspended in FACS buffer and
676 incubated with a panel of fluorophore-conjugated anti-mouse antibodies consisting of anti-
677 CD45, anti-CD3e, anti-CD4, anti-CD8α, anti-PD-1, and anti-Tim3 (Havcr2/CD366)
678 antibodies (Table S27A) before being analyzed by BD FACSAria III (BD Biosciences).
679
680 **Bulk-RNA sequencing**
681 Mouse livers were harvested 30 days post-injection. Tumor-infiltrating leukocytes yielded
682 by the same procedure as that used for flow cytometry were utilized for the CD45-positive
683 leukocyte selection. 10 μL of CD45 microbeads (Miltenyi Biotec, #130-052-301) was mixed
684 well and incubated with each $1x10^7$ cells in 90 μL of FACS buffer for 30mins at 4ºC. The
685 CD45-positive selection was then conducted using the MACS LS column and the
686 MidiMACS separator (Miltenyi Biotec), following the column-based magnetic cell-
687 separation strategy established by the manufacturer. $CD4^+$ TILs and $CD8^+$ TILs were
688 identified using a panel of fluorophore-conjugated anti-mouse antibodies consisting of CD45,
689 CD3e, CD4, and CD8α, and isolated by BD FACSAria III Cell Sorter (BD Biosciences).

690 Total RNA was isolated using RNeasy Micro Kit (Qiagen). RNA integrity number
691 (RIN) values were measured using the Agilent 2100 Bioanalyzer (Agilent Technologies).
692 Samples with RIN > 7 were subsequently used for library preparation using the SMARTer
693 Stranded Total RNA-seq Kit v2 - Pico Input Mammalian (Takara Inc.) according to the
694 manufacturer's protocol. The library size distribution and concentration were assessed with
695 the High Sensitivity DNA assay using the Agilent 2100 Bioanalyzer (Agilent Technologies).
696 Sequencing was carried out using the Illumina HiSeq X platform (Macrogen) with a standard
697 150 bp paired-end read protocol. Subsequently, the gene expression was analyzed from the
698 sequencing data using the CLC workbench version 11.0.1 (Qiagen) according the procedure
699 described previously[73]. DEGs were identified by the Differential Expression for RNA-Seq
700 tool of CLC workbench using the Wald test applying for the Against-control-group
701 comparison with the *Tet2*$^{fl/fl}$ group serving as the control. The gene expression datasets were
702 then used to identify significantly enriched gene sets for each group using GSEA[42] (GSEA
703 4.3.0, https://www.gsea-msigdb.org/gsea/index.jsp) with the ImmuneSigDB subset of C7
704 (4872 gene sets, https://www.gsea-msigdb.org/gsea/msigdb/human/collections.jsp) for
705 annotation.
706
707 **Upstream regulator analysis**
708 Overlapping downregulated DEGs within CD8$^{+}$ TILs from *Vav1*$^{Cre}$*Tet2KO* and
709 *Cd4*$^{Cre}$*Tet2KO* groups compared to the *Tet2*$^{fl/fl}$ group (FDR< 0.05, Log2 FC < -1; Table S8)
710 were used to predict the upstream transcription factors by the Upstream Regulator Analysis
711 function of QIAGEN's IPA[74] (QIAGEN Redwood City, www.qiagen.com/ingenuity). The

712 pathway analysis was performed using the core analysis based on gene expression fold
713 change[74]. The upstream transcription regulators were called with overlap p-value < 0.01. The
714 extracted upstream regulators were then used to generate the molecular interaction network
715 by the Network and Pathway tools of IPA.
716
717 **Indirect immunofluorescence staining, co-expression cell evaluation**
718 Liver metastasis tissue collected from *Vav1*$^{Cre}$*Tet2KO, Cd4*$^{Cre}$*Tet2KO* and *Tet2*$^{fl/fl}$ groups
719 were mounted in O.C.T embeding compound (Sakura Finetek Japan Co.), frozen rapidly in
720 hexane-dry ice and stored at -80$^{o}$C. The frozen tissue blocks were then sectioned at 4 µm-
721 thickness in a cryostat at -20$^{o}$C. Sections were dried up in air for 60 mins at room temperature
722 (RT), fixed in 4% paraformaldehyde for 15 mins and permeabilized in 0.1% Triton X100 for
723 10 mins and incubated with protein blocking buffer (Protein block, Abcam, #ab64226).
724 Sections were then incubated with primary antibodies at 4$^{o}$C for 16 hours, washed 3 times in
725 PBS for 5 mins each and subsequently incubated with secondary antibodies for 30 mins at
726 RT. Antibodies and the dilution used for immunofluorescence staining were provided in the
727 Table S27D. After three washes, tissue sections were incubated with True VIEW
728 Autofluorescence Quenching Kit (Vector Laboratories, #SP-8400-15) for 5 mins at RT and
729 mounted with 4',6-diamidino-2- 129 phenylindole (DAPI, Vectashield Mounting Medium;
730 Vector Laboratories, #H-1200).
731 The sections were imaged using the confocal laser scanning microscope (Leica TCS
732 SP8, Leica Microsystems). To quantify exhaustion phenotypes, CD8$^{+}$ TILs co-expressing
733 PD-1, Tim3, or Tox were manually counted in 10 to 20 random intratumoral fields per sample

734 at 40× magnification. Data were expressed as the percentage of each subset relative to the
735 total $CD8^+$ TIL population. The one-way ANOVA test with $\alpha = 0.05$ was used to compare
736 the percentage of co-expressing cells between groups.
737
738 **Single-cell RNA sequencing (scRNA-seq) library preparation, data acquisition and pre-**
739 **processing**
740 Liver samples from *Vav1*$^{Cre}$*Tet2KO* mice and *Tet2*$^{fl/fl}$ mice were harvested at day 30 post-
741 injection, and tumor-infiltrating leukocytes were harvested using the cell processing
742 procedure that used for flow cytometry. The yielded cells were washed and resuspended in
743 PBS supplemented with 1% BSA. Cells were then incubated with Brilliant Violet 421
744 (BV421) anti-mouse CD45.2 antibody (clone 104, Biolegend, #109832) for 20 minutes at
745 4°C, followed by staining with 7-AAD viability solution (ThermoFisher Scientific, 00-6993-
746 50; 1:20) for 10 minutes on ice. CD45-positive live cells were subsequently sorted using the
747 BD FACSAria III (BD Biosciences). Isolated CD45+ live cells were processed to generate
748 barcoded 5′ gene expression (5′ GEX) libraries, together with T-cell receptor (TCR)-enriched
749 libraries, using the Chromium Next GEM Single Cell V(D)J Reagent Kits v1.1 (10x
750 Genomics, Pleasanton, CA, USA). The procedure followed the manufacturer's instructions
751 (CG000208 Rev G) and aimed to capture 10,000 cells per library. All libraries were subjected
752 to quality 150 control checks and quantified using the 2100 Bioanalyzer High Sensitivity
753 DNA Kit (Agilent 151 Technologies) and KAPA Library Quantification kit for Illumina
754 platforms (Kapa Biosystems, KK4873). The library were sequenced on the Illumina

755 NovaSeqX Plus Sequencing System (Macrogen), then mapped to the mouse genome
756 (GRCm39) and demultiplexed using CellRanger (10X Genomics, v.8.0.1).
757
758 **scRNA-seq data processing of individual samples**
759 Matrix data of each samle was processed using Seurat[75] (v.5.1.0) in RStudio (v.4.4.1).
760 Doublets were detected and removed using the "scDblFinder" function from the scDblFinder
761 package[76] (v.1.18.0) with the default estimated doublet rate. Cells with fewer than 200 or
762 more than 2,500 unique genes and those with over 5% of mitochondrial gene reads were
763 excluded. After removing ribosomal and mitochondrial genes, gene expression count data
764 was normalized using the "NormalizeData" function. Normalized data were linearly
765 transformed (scaled) with the "ScaleData" function and subjected to principal component
766 analysis (PCA) via the "RunPCA" function. Graph-based clustering was performed based on
767 gene expression profiles using the "FindNeighbors" and "FindClusters" functions. Clusters
768 were visualized using Uniform Manifold Approximation and Projection (UMAP) technique
769 via the "RunUMAP" and "DimPlot" functions.
770 Cell clusters were annotated as T lymphocytes, B lymphocytes, NK cells, and
771 myeloid cells based on marker genes identified by the "FindAllMarkers" and
772 "FindConservedMarkers" functions. For a gene to be considered a marker, a minimum of
773 25% gene-expressing cells per cluster was required, and the minimum Log2 FC in gene
774 expression of each cluster, compared to all other clusters, was set to 0.25.
775
776 **Data integration for scRNA-seq and batch correction**

777 Canonical correlation analysis (CCA) was performed to identify shared features across
778 multiple gene expression datasets using the FindIntegrationAnchors function of Seurat. Four
779 datasets (data from tumor-infiltrating leukocytes of *Tet2*$^{fl/fl}$ ($n$ = 2) and *Vav1*$^{Cre}$*Tet2KO* ($n$ =
780 2) mice) were integrated based on the identified anchors using the IntegrateData function
781 with 30 canonical correlation dimensions. The integrated data were scaled, subjected to PCA,
782 and used for graph-based clustering for cell annotation, as described above.
783

784 **scRNA-seq subclustering and cell-type annotation**

785 CD8$^+$ TIL clusters were identified and extracted from the integrated data, followed by scaling,
786 PCA-based dimensionality reduction, and unsupervised graph-based subclustering for cell
787 annotation. Subclusters that highly expressed marker genes characteristic of other immune
788 cell subsets, distinct from CD8$^+$ TILs, were excluded. Following in silico sorting, the CD8
789 T-cell dataset comprised 2,251 *Vav1*$^{Cre}$*Tet2KO* CD8$^+$ TILs and 1,101 *Tet2*$^{fl/fl}$ CD8$^+$ TILs. To
790 minimize discrepancies in cell numbers between the groups, downsampling was performed,
791 resulting in a balanced dataset of 1,101 CD8$^+$ TILs per group. The downsampling process
792 was repeated multiple times to ensure consistency with the original data. Cell subclusters
793 were annotated by analyzing the expression levels of canonical gene markers using Seurat's
794 "FindAllMarkers" and "FindConservedMarkers" functions.
795

796 **DEG analysis of scRNA-seq**

797 DEG analysis between *Tet2*$^{fl/fl}$ and *Vav1*$^{Cre}$*Tet2KO* conditions was performed using
798 "FindMarkers" function of Seurat. Genes were considered differentially expressed if they

799 met the following criteria: (i) expressed in a minimum of 10% of cells per cluster within at
800 least one condition, and (ii) exhibited a Benjamini–Hochberg adjusted p-value (adjusted p-
801 value) less than 0.05.
802
803 **Analysis of single-cell gene set activity**
804 We used the gene set comprising of 42 consistently exhausted T cell associated marker genes
805 identified by Zhang[45] to calculate the T-cell exhaustion score for single cell $CD8^+$ TIL dataset
806 using "AddModuleScore" function. The number of bins of aggregate expression levels for
807 all analyzed features was set to 24 and number of control features selected from the same bin
808 per analyzed feature was set to 100. The differential enrichment of T-cell exhaustion scores
809 between *Tet2*$^{fl/fl}$ and *Vav1*$^{Cre}$*Tet2KO* groups was visualized using boxplots, and statistical
810 significance was assessed via the Mann-Whitney U test.
811 We used the AUCell package[44] v.1.26.0 to analyze the Memory versus Exhausted
812 CD8 T-cell signature enrichment, and Effector versus Exhausted CD8 T-cell signature
813 enrichment for $CD8^+$ TIL dataset. The gene set
814 "*GSE9650_EXHAUSTED_VS_MEMORY_CD8_TCELL_DN"* and "*GSE9650*
815 *_EXHAUSTED_VS_MEMORY_CD8_TCELL_UP*" were obtained from the Human MSigDB
816 (v2024.1.Hs) and converted to mouse orthologs using the 'orthologs" function from the
817 babelgene package (v.22.9). Gene expression rankings were calculated for each cell using
818 the "AUCell_buildRankings" function, followed by computation of the area under the curve
819 (AUC) scores of every cells for each gene set using the "AUCell_calcAUC" function. To
820 create an aggregate Memory versus Exhausted CD8 T-cell signature, the AUC values of the

821 upregulated gene set were subtracted from those of the downregulated gene set. Similarly, to
822 calculate the aggregate Effector versus Exhausted CD8 T-cell signature enrichment, we
823 subtracted the AUC values of the downregulated gene set from those of the upregulated gene
824 set using the gene sets "GSE9650_EFFECTOR_VS_EXHAUSTED_CD8_TCELL_DN"
825 and "GSE9650_EFFECTOR_VS_EXHAUSTED_CD8_TCELL_UP" obtained from the
826 Human MSigDB (v2024.1.Hs). The differential enrichments of these gene signatures
827 between *Tet2*$^{fl/fl}$ and *Vav1*$^{Cre}$*Tet2KO* groups were visualized using boxplots, and statistical
828 significance was assessed via the Mann-Whitney U test.
829
830 **Single-cell trajectory inference**
831 We used *Monocle 3 toolkit*[46] (v.1.3.7) to construct the cellular pseudotime trajectories for
832 CD8 T-cell subsets. Single cell datasets were preprocessed using PCA, retaining 50
833 dimensions. Dimensionality reduction was then performed using UMAP technique. Cells
834 were clustered using the "cluster_cells" function with the Leiden algorithm, setting the
835 resolution parameter to 0.008, the number of nearest neighbors (k) to 20, and performing two
836 iterations. A principal graph representing cellular transitions was learned using the
837 "learn_graph" function with default heuristics and without partitioning the data. According
838 to previous knowledge, we selected the root cell cluster to order single cells along the
839 trajectory using the "order_cells" function. Single cell pseudotime and trajectory were
840 visualized using the "plot_cells" function.
841
842 **TCR-seq data analysis**

843 Single cell TCR-seq contig data from all samples were combined and annotated into
844 clonotypes based on shared nucleotide sequences, amino acid sequences, and V(D)J gene
845 segment usage using the "combineTCR" function of scRepertoire package[47] (v.2.3.0).
846 Clonotypes were defined using the combination of V(D)J genes (TCR/Ig) and the nucleotide
847 sequence of the CDR3 region (strict clonotype calling) throughout the analysis. The
848 clonotype data was integrated with gene expression datasets for clonal frequency calculation
849 using the "combineExpression" function. TCR clonotype similarity across cell clusters was
850 analyzed using the "clonalOverlap" function with the Morisita overlap index[47].

851 Clonal diversity was quantified using Shannon entropy and the inverse Simpson
852 index[77,78]. Clonal inequality was assessed using the Gini coefficient and Lorenz curve
853 analysis[79]. All metrics were calculated from TCR clonotype frequencies using R (v.4.4.1) in
854 RStudio.

855

856 **Whole genome bisulfite sequencing (WGBS)**

857 PD-1$^{+}$CD8$^{+}$ TILs isolated from the liver metastatic tumors of *Vav1*$^{Cre}$*Tet2KO* ($n$ = 3) and
858 *Tet2*$^{fl/fl}$ ($n$ = 3) mice were used for library preparation. Genomic DNA for WGBS was
859 extracted from sorted cells using the QIAamp DNA Blood Mini Kit (Qiagen). The library for
860 WGBS was prepared using the postbisulfite adaptor tagging (PBAT) protocol as described
861 previously[80,81]. After library preparation, library yields were quantified using the library
862 quantification kit (Takara Bio Inc.) and amplified using PrimeStar Max DNA polymerase
863 (Takara Bio Inc.). The amplified libraries were sequenced on the Illumina HiSeq X platform
864 at Macrogen.

865 WGBS data were aligned to the *Mus musculus* reference genome (GRCm39) using
866 the Bismark pipeline[82]. Differentially methylated region (DMR) analysis was performed
867 using *methylKit* package (v.1.30.0). For the genome-wide analysis, DMRs of *Tet2KO* PD-
868 $1^+CD8^+$ TILs in comparison to *Tet2*$^{fl/fl}$ PD-$1^+CD8^+$ TILs were detected by scanning non-
869 overlapping 1000bp-windows across the whole genome locus using the calculateDiffMeth
870 and getMethylDiff functions, applying a q-value $< 0.01$ and $|\text{meth.diff}| \geq 20\%$. For DMR
871 analysis focusing *Tox* gene, DMRs were detected by screening 500bp-windows at 250bp-
872 step, applying the same statistical thresholds as in the global analysis. Differentially
873 methylated cytosines (DMCs) within the *Tox* locus were identified at single-CpG resolution
874 with the same q-value and methylation difference cutoffs. DMRs were annotated using the
875 annotatePeakInBatch function from the ChIPpeakAnno package (v3.38), with mouse gene
876 annotations from the Gencode vM35 primary assembly and the ENCODE Registry of cCREs
877 (v3, 2021) serving as reference. DMRs overlapping enhancer, promoter, CTCF, or TSS
878 regions were classified as regulatory DMRs (rDMRs).

879 To quantify the combined regulatory impact of differential methylation on gene
880 expression, we developed a composite methylation impact score that accounts for both the
881 breadth (number of affected regulatory elements) and depth (magnitude of methylation
882 changes) of regulatory disruption. The impact score for each gene was calculated as:

883 $$\text{Impact Score} = (\text{Total regulatory DMRs}) \times (\text{Mean absolute methylation difference})$$

884 Where:

885 Total regulatory DMRs: the number of differentially methylated regions
886 (qvalue < 0.01, |methylation difference| ≥ 20%) overlapping with any regulatory
887 element (promoter, TSS, enhancer, or CTCF binding site) associated with the gene.

888 Mean absolute methylation difference: the average magnitude of methylation
889 change (%) across all regulatory DMRs for that gene.

890 This scoring approach identifies genes with extensive regulatory methylation
891 changes that are likely to have substantial effects on transcriptional control. Genes with
892 higher scores have both multiple affected regulatory elements and large-magnitude
893 methylation changes.

894

895 ***In vivo* anti-PD-1 blockade**

896 Anti-PD-1 antibody treatment was started seven days after the intrasplenic injection of
897 Venus-*AKTP*$^{M/LOH}$ cells. InVivoMAb anti-mouse PD-1 (RMP1-14, Bio X Cell, #BE0146)
898 was diluted with PBS to a final concentration of 1 μg/μL and intraperitoneally injected at a
899 dose of 10 μg/g of mouse body weight every 3 days for 6 doses in total. Control mice received
900 InVivoMAb rat IgG2a isotype control (2A3, Bio X Cell, #815022F1) following the same
901 dilution and dosage as the anti-PD-1 antibody treatment protocol. Mice were sacrificed 30
902 days after the injection of Venus-*AKTP*$^{M/LOH}$ cells to collect the whole liver for LMTB
903 evaluation.

904

905 **Competitive bone marrow transplantation (BMT) mouse model with CRC liver**
906 **metastasis**

907 Bone marrow isolation and preparation: Bone marrow cells were harvested from femurs and
908 tibias of 8-10 week-old donor mice. Bones were flushed with ice-cold PBS containing 2%
909 FBS using a 23-gauge needle. Cell suspensions were filtered through 70-μm cell strainers.
910 Viable cell counts were determined by trypan blue exclusion.

911 Lethal irradiation and competitive transplantation: Recipient CD45.1$^{+}$ C57BL/6J
912 mice (8-12 weeks old) were lethally irradiated using an X-ray irradiator (Hitachi Power
913 Solutions MBR-1520R-3) with a split-dose protocol of 4.5 Gy twice, administered 4 hours
914 apart (total dose of 9.0 Gy) while housed in pie cages to ensure uniform radiation exposure.
915 For *Tet2KO:Tet2WT* chimeras, *Vav1Cre*$^{+}$*Tet2*$^{fl/fl}$ CD45.2$^{+}$ bone marrow cells were mixed
916 with *Tet2WT* CD45.1$^{+}$/CD45.2$^{+}$ competitor bone marrow cells at ratios of 1:2 or 1:3. Control
917 *Tet2*$^{fl/fl}$*:Tet2WT* chimeras received a 1:1 mixture of *Tet2*$^{fl/fl}$ CD45.2$^{+}$ and *Tet2WT*
918 CD45.1$^{+}$/CD45.2$^{+}$ bone marrow cells. A total of $2\times10^{6}$ bone marrow cells in 200 μL PBS
919 were injected via retro-orbital venous plexus within 4-6 hours post-irradiation. Mice were
920 maintained in sterilized caging, food, and water were provided during the first 14 days after
921 transplantation.

922 Chimerism was assessed in peripheral blood collected via facial vein bleeding at 4
923 weeks and re-evaluated at 12 weeks post-BMT to confirm the proliferative advantage of
924 *Tet2KO* hematopoietic and lymphoid compartments. Donor cell engraftment was quantified
925 by flow cytometry analysis of CD45.1 and CD45.2 expression.

926 After confirming adequate hematopoietic reconstitution at four weeks post-BMT,
927 Venus-*AKTP*$^{M/LOH}$ cells were injected intrasplenically to establish liver metastases. Eight
928 weeks after cancer cell injection, mice were euthanized and livers were harvested and
929 processed for histological analysis. LMTB was quantified by microscopic measurement as
930 described above. Tumor-infiltrating immune cells were isolated from liver metastases by
931 enzymatic digestion as described above and subsequently analyzed by flow cytometry to
932 identify exhausted T-cell populations using a panel of fluorophore-conjugated anti-mouse
933 antibodies, consisting of anti-CD3ε, anti-CD4, anti-CD8α, anti-PD-1, anti-Tim3
934 (Havcr2/CD366), anti-CD45.1, and anti-CD45.2 antibodies (see Table S27B).
935

936 ***In vitro* modeling of CD8 T-cell exhaustion**

937 CD8 T cells were isolated from spleens of *CD4*$^{Cre}$*Tet2KO* mice, and *Tet2*$^{fl/fl}$ mice using the
938 Mouse CD8 T Cell Isolation Kit (Miltenyi Biotec, # 130-095-236) according to the
939 manufacturer's instructions. Purity (>90% $CD45^+CD3^+CD8^+$ cells) was confirmed by flow
940 cytometry.

941 Purified CD8 T cells were seeded at $2\times10^7$ cells per well in 6-well plates and activated
942 with plate-bound anti-CD3ε antibody (2 μg/mL, clone 145-2C11, BioLegend, #100340) and
943 soluble anti-CD28 antibody (2 μg/mL, clone 37.51, BioLegend, #102116) in complete RPMI
944 1640 medium supplemented with 10% FBS, 1% penicillin-streptomycin, 50 μM β-
945 mercaptoethanol, 10 mM HEPES, and recombinant mouse IL-2 (125 U/mL, PeproTech,
946 #212-12). After 4 days, T cells were harvested and transferred to fresh wells pre-coated with
947 anti-CD3 antibody alone (2 μg/mL) for chronic re-stimulation. This re-stimulation was

948 repeated on day 8. T cells were cultured for a total of 12-14 days at 37°C with 5% $CO_2$, with
949 medium containing IL-2 (125 U/mL) refreshed every 2-3 days.

950 At indicated timepoints (days 7 and 12), T cells were harvested and assessed for
951 exhaustion markers by flow cytometry using panels of fluorophore-conjugated anti-mouse
952 antibodies, consisting of anti-CD3ε, anti-CD8α, anti-PD-1, anti-Tim3 (Havcr2/CD366), and
953 anti-Tcf1 antibodies (see Table S27C). For intracellular staining, cells were first stained with
954 Fixable Viability Dye eFluor 780 (eBioscience, #65-0865-14), followed by cell-surface
955 markers. Cells were then fixed and permeabilized using the Foxp3/Transcription Factor
956 Staining Buffer Set (eBioscience, #00-5523-00) according to the manufacturer's instructions,
957 and stained with intracellular antibodies for 30 minutes at room temperature. Data were
958 acquired on BD FACSAria III and analyzed using FlowJo software (BD Biosciences).
959

960 **Acknowledgements**

961 We thank the staff of the associated institutions and departments for their technical assistance
962 throughout this project. We are grateful to the staff of the University of Tsukuba Animal
963 Resource Center for their support with animal care. The authors also thank Editage
964 (www.editage.com) for language editing. Figures were created using BioRender.com.

965 This work was supported by Grants-in-Aid for Scientific Research (KAKENHI:
966 JP25K19551 [M.F.], JP25K19567 [S.S.], JP25K19550 [Y.S.], JP23K15293 [K.M.], and
967 JP25H01055 [M.S.-Y.]) from the Ministry of Education, Culture, Sports, and Science of
968 Japan; AMED (JP256f0137008 [M.F.], JP23tk0124002, JP24ck0106908, JP23ck0106797,
969 JP22H04925 (PAGS), JP22zf0127009 (the Moonshot Research and Development Program)

970 and JP25gm2010006 (CREST) [M.S.-Y.]); Kobayashi Foundation for Cancer Research,
971 Japan Leukemia Research Fund, and Takeda Science [S.S.], and The Uehara Memorial
972 Foundation, Takeda Science, Kobayashi Foundation for Cancer Research, Kobayashi
973 Foundation, and the Chemo-Sero Therapeutic Research Institute [M.S.-Y.]. M.F. was
974 supported by Gilead's Research Scholars Program and a grant from The Leukemia &
975 Lymphoma Society (Grant ID: 3442-25). G.C. was supported by the National Sciences and
976 Engineering Research Council of Canada (Award 618788). R.J.V. reports funding from
977 Canadian Institutes for Health Research (PJT 203869, PJF 204160), The Princess Margaret
978 Cancer Foundation, The Leukemia and Lymphoma Society of Canada (1445410), the Brain
979 Tumour Foundation of Canada, Lymphoma Canada, Marathon of Hope Cancer Centres
980 Network Clinician Scientist Award (3256-04), Brain Canada and Cancer Research Society
981 Translational Research Grant in Brain Cancer, Cancer Research Society (1455586), and a
982 University of Toronto Hold 'Em For Life Early Career Professorship. The funders had no
983 role in the study design, data collection and analysis, or decision to publish or prepare the
984 manuscript.

985

986 **Author contributions**

987 **Conceptualization**: M.S.-Y and R.J.V.. **Data Curation**: A.N.T.L., M.F., G.C., R.J.V.,
988 T.B.N., S.S., Y.S., F.M., H.A., Y.T.M.N. **Formal analysis**: A.N.T.L., R.J.V., T.B.N., and
989 M.F. **Funding acquisition**: M.F., Y.S., K.M., R.J.V., and M.S.-Y. **Investigation**: A.N.T.L.,
990 T.B.N., Y.T.M.N., G.C. **Methodology**: A.N.T.L., T.B.N., M.F., R.J.V., F.M., H.A., H.O.,
991 M.N., M.K., M.O., and M.S.-Y. **Project administration**: A.N.T.L., M.F., R.J.V., and M.S.-

Y. **Resources**: A.N.T.L., M.F., T.B.N., G.C., Y.T.M.N., F.M., H.A., S.S., K.M., T.S., H.O., M.N., M.O., S.I., S.S., Y.S., M.K., R.J.V., and M.S.-Y. **Software**: A.N.T.L., R.J.V., M.F., and T.B.N. **Supervision**: M.F., R.J.V., and M.S.-Y. **Validation**: A.N.T.L., R.J.V., and T.B.N. **Visualization**: A.N.T.L., R.J.V., and M.F. **Writing-Original Draft**: A.N.T.L., R.J.V., M.F., and M.S.-Y. **Writing-Review & Editing**: A.N.T.L., M.F., R.J.V., G.C., and M.S.-Y.

### Declaration of Interests

M.F. received research support from Gilead Sciences (Research Scholars Program) and The Leukemia & Lymphoma Society. M.S.-Y. received research support from the Takeda Science Foundation and the Chemo-Sero Therapeutic Research Institute. R.J.V. is co-inventor on a patent, “Clonal Hematopoiesis as a Biomarker”. The authors declare no other competing interests.

### Declaration of generative AI and AI-assisted technologies

During manuscript preparation, generative AI tools were used solely for language editing and clarity improvement. The authors reviewed and validated all content and take full responsibility for the manuscript.

## RESOURCE AVAILABILITY

### Lead contact

Further information and requests for resources and reagents should be directed to and will be fulfilled by the lead contact, Mamiko Sakata-Yanagimoto (sakatama@md.tsukuba.ac.jp).

**Materials availability**

This study did not generate new unique reagents.

**Data and code availability**

Statistical source data and detailed results for human cohort analyses (Figure 1 and Figure S1) are provided in Table S1 and Table S2. All original code will be deposited at GitHub and made publicly available as of the date of publication. The code for scRNA-seq and WGBS analysis will be available at: [Link will be provided upon publication]. The code for clonal hematopoiesis correlation analysis is available at: https://github.com/GiacomoCampo/msk_ch_correlations. Any additional information required to reanalyze the data reported in this paper is available from the lead contact upon request.

1024 **REFERENCES**


1025 1. Luyendijk, M., Visser, O., Blommestein, H.M., de Hingh, I., Hoebers, F.J.P., Jager, A., Sonke,
1026 G.S., de Vries, E.G.E., Uyl-de Groot, C.A., and Siesling, S. (2023). Changes in survival in de
1027 novo metastatic cancer in an era of new medicines. J Natl Cancer Inst *115*, 628-635.
1028 10.1093/jnci/djad020.

1029 2. Kitamura, T., Qian, B.Z., and Pollard, J.W. (2015). Immune cell promotion of metastasis.
1030 Nat Rev Immunol *15*, 73-86. 10.1038/nri3789.

1031 3. Edwards, S.C., Hoevenaar, W.H.M., and Coffelt, S.B. (2021). Emerging immunotherapies
1032 for metastasis. British Journal of Cancer *124*, 37-48. 10.1038/s41416-020-01160-5.

1033 4. Arias-Badia, M., Chang, R., and Fong, L. (2024). γδ T cells as critical anti-tumor immune
1034 effectors. Nature Cancer *5*, 1145-1157. 10.1038/s43018-024-00798-x.

1035 5. Dean, I., Lee, C.Y.C., Tuong, Z.K., Li, Z., Tibbitt, C.A., Willis, C., Gaspal, F., Kennedy, B.C.,
1036 Matei-Rascu, V., Fiancette, R., et al. (2024). Rapid functional impairment of natural killer
1037 cells following tumor entry limits anti-tumor immunity. Nature Communications *15*, 683.
1038 10.1038/s41467-024-44789-z.

1039 6. Portale, F., and Di Mitri, D. (2023). NK Cells in Cancer: Mechanisms of Dysfunction and
1040 Therapeutic Potential. Int J Mol Sci *24*. 10.3390/ijms24119521.

1041 7. Xie, F., Zhou, X., Su, P., Li, H., Tu, Y., Du, J., Pan, C., Wei, X., Zheng, M., Jin, K., et al. (2022).
1042 Breast cancer cell-derived extracellular vesicles promote CD8+ T cell exhaustion via TGF-β
1043 type II receptor signaling. Nature Communications *13*, 4461. 10.1038/s41467-022-31250-
1044 2.

1045 8. Baessler, A., and Vignali, D.A.A. (2024). T Cell Exhaustion. Annu Rev Immunol *42*, 179-206.
1046 10.1146/annurev-immunol-090222-110914.

1047 9. Gavil, N.V., Scott, M.C., Weyu, E., Smith, O.C., O'Flanagan, S.D., Wijeyesinghe, S., Lotfi-
1048 Emran, S., Shiao, S.L., Vezys, V., and Masopust, D. (2023). Chronic antigen in solid tumors
1049 drives a distinct program of T cell residence. Sci Immunol *8*, eadd5976.
1050 10.1126/sciimmunol.add5976.

1051 10. Coffelt, S.B., Kersten, K., Doornebal, C.W., Weiden, J., Vrijland, K., Hau, C.-S., Verstegen,
1052 N.J.M., Ciampricotti, M., Hawinkels, L.J.A.C., Jonkers, J., and de Visser, K.E. (2015). IL-17-
1053 producing γδ T cells and neutrophils conspire to promote breast cancer metastasis. Nature
1054 *522*, 345-348. 10.1038/nature14282.

1055 11. Wu, P., Wu, D., Ni, C., Ye, J., Chen, W., Hu, G., Wang, Z., Wang, C., Zhang, Z., Xia, W., et al.
1056 (2014). γδT17 cells promote the accumulation and expansion of myeloid-derived
1057 suppressor cells in human colorectal cancer. Immunity *40*, 785-800.
1058 10.1016/j.immuni.2014.03.013.

1059 12. Hedrick, C.C., and Malanchi, I. (2022). Neutrophils in cancer: heterogeneous and
1060 multifaceted. Nature Reviews Immunology *22*, 173-187. 10.1038/s41577-021-00571-6.

1061 13. de Visser, K.E., and Joyce, J.A. (2023). The evolving tumor microenvironment: From cancer
1062 initiation to metastatic outgrowth. Cancer Cell *41*, 374-403. 10.1016/j.ccell.2023.02.016.

1063 14. Xu, J., Ding, L., Mei, J., Hu, Y., Kong, X., Dai, S., Bu, T., Xiao, Q., and Ding, K. (2025). Dual
1064 roles and therapeutic targeting of tumor-associated macrophages in tumor
1065 microenvironments. Signal Transduction and Targeted Therapy *10*, 268. 10.1038/s41392-
1066 025-02325-5.

1067 15. Herbrich, S., Chaib, M., Anandhan, S., Andrewes, S.W., Nagarajan, A., Guan, B., Gandhi, N.,
1068 Gilliam, J., Radovich, M., and Sharma, P. (2026). *TET2* mutant clonal hematopoiesis
1069 enhances macrophage antigen presentation and improves immune checkpoint therapy in
1070 solid tumors. Cancer Cell *44*, 187-202.e187. 10.1016/j.ccell.2025.09.011.

1071 16. Carnevale, S., Di Ceglie, I., Grieco, G., Rigatelli, A., Bonavita, E., and Jaillon, S. (2023).
1072 Neutrophil diversity in inflammation and cancer. Front Immunol *14*, 1180810.
1073 10.3389/fimmu.2023.1180810.

1074 17. Jaillon, S., Ponzetta, A., Di Mitri, D., Santoni, A., Bonecchi, R., and Mantovani, A. (2020).
1075 Neutrophil diversity and plasticity in tumour progression and therapy. Nat Rev Cancer *20*,
1076 485-503. 10.1038/s41568-020-0281-y.

1077 18. Sebestyen, Z., Prinz, I., Déchanet-Merville, J., Silva-Santos, B., and Kuball, J. (2020).
1078 Translating gammadelta (γδ) T cells and their receptors into cancer cell therapies. Nature
1079 Reviews Drug Discovery *19*, 169-184. 10.1038/s41573-019-0038-z.

1080 19. Bruni, E., Cimino, M.M., Donadon, M., Carriero, R., Terzoli, S., Piazza, R., Ravens, S., Prinz,
1081 I., Cazzetta, V., Marzano, P., et al. (2022). Intrahepatic CD69(+)Vδ1 T cells re-circulate in
1082 the blood of patients with metastatic colorectal cancer and limit tumor progression. J
1083 Immunother Cancer *10*. 10.1136/jitc-2022-004579.

1084 20. Wu, Y., Kyle-Cezar, F., Woolf, R.T., Naceur-Lombardelli, C., Owen, J., Biswas, D., Lorenc, A.,
1085 Vantourout, P., Gazinska, P., Grigoriadis, A., et al. (2019). An innate-like Vδ1(+) γδ T cell
1086 compartment in the human breast is associated with remission in triple-negative breast
1087 cancer. Sci Transl Med *11*. 10.1126/scitranslmed.aax9364.

1088 21. Jaiswal, S., and Ebert, B.L. (2019). Clonal hematopoiesis in human aging and disease.
1089 Science *366*, eaan4673. doi:10.1126/science.aan4673.

1090 22. Bolton, K.L., Ptashkin, R.N., Gao, T., Braunstein, L., Devlin, S.M., Kelly, D., Patel, M.,
1091 Berthon, A., Syed, A., Yabe, M., et al. (2020). Cancer therapy shapes the fitness landscape
1092 of clonal hematopoiesis. Nature Genetics *52*, 1219-1226. 10.1038/s41588-020-00710-0.

1093 23. Coombs, C.C., Zehir, A., Devlin, S.M., Kishtagari, A., Syed, A., Jonsson, P., Hyman, D.M.,
1094 Solit, D.B., Robson, M.E., and Baselga, J. (2017). Therapy-related clonal hematopoiesis in
1095 patients with non-hematologic cancers is common and associated with adverse clinical
1096 outcomes. Cell stem cell *21*, 374-382. e374.

1097 24. Kleppe, M., Comen, E., Wen, H.Y., Bastian, L., Blum, B., Rapaport, F.T., Keller, M., Granot,
1098 Z., Socci, N., Viale, A., et al. (2015). Somatic mutations in leukocytes infiltrating primary
1099 breast cancers. npj Breast Cancer *1*, 15005. 10.1038/npjbcancer.2015.5.

1100 25. Severson, E.A., Riedlinger, G.M., Connelly, C.F., Vergilio, J.A., Goldfinger, M., Ramkissoon,
1101 S., Frampton, G.M., Ross, J.S., Fratella-Calabrese, A., Gay, L., et al. (2018). Detection of

1102 clonal hematopoiesis of indeterminate potential in clinical sequencing of solid tumor
1103 specimens. Blood *131*, 2501-2505. 10.1182/blood-2018-03-840629.

1104 26. Marshall, C.H., Gondek, L.P., Luo, J., and Antonarakis, E.S. (2022). Clonal Hematopoiesis of
1105 Indeterminate Potential in Patients with Solid Tumor Malignancies. Cancer Res *82*, 4107-
1106 4113. 10.1158/0008-5472.Can-22-0985.

1107 27. Pich, O., Bernard, E., Zagorulya, M., Rowan, A., Pospori, C., Slama, R., Huerga Encabo, H.,
1108 O'Sullivan, J., Papazoglou, D., Anastasiou, P., et al. (2025). Tumor-Infiltrating Clonal
1109 Hematopoiesis. New England Journal of Medicine *392*, 1594-1608.
1110 10.1056/NEJMoa2413361.

1111 28. Buttigieg, M.M., Vlasschaert, C., Bick, A.G., Vanner, R.J., and Rauh, M.J. (2025).
1112 Inflammatory reprogramming of the solid tumor microenvironment by infiltrating clonal
1113 hematopoiesis is associated with adverse outcomes. Cell Rep Med *6*, 101989.
1114 10.1016/j.xcrm.2025.101989.

1115 29. Pan, W., Zhu, S., Qu, K., Meeth, K., Cheng, J., He, K., Ma, H., Liao, Y., Wen, X., Roden, C., et
1116 al. (2017). The DNA Methylcytosine Dioxygenase Tet2 Sustains Immunosuppressive
1117 Function of Tumor-Infiltrating Myeloid Cells to Promote Melanoma Progression. Immunity
1118 *47*, 284-297.e285. https://doi.org/10.1016/j.immuni.2017.07.020.

1119 30. Nguyen, Y.T.M., Fujisawa, M., Nguyen, T.B., Suehara, Y., Sakamoto, T., Matsuoka, R., Abe,
1120 Y., Fukumoto, K., Hattori, K., Noguchi, M., et al. (2021). Tet2 deficiency in immune cells
1121 exacerbates tumor progression by increasing angiogenesis in a lung cancer model. Cancer
1122 Sci *112*, 4931-4943. 10.1111/cas.15165.

1123 31. Krishnan, T., Solar Vasconcelos, J.P., Titmuss, E., Topham, J.T., Schaeffer, D.F., Karsan, A.,
1124 Lim, H.J., Ho, C., Gill, S., Kennecke, H.F., et al. (2024). Clonal hematopoiesis of
1125 indeterminate potential (CHIP), treatment outcomes and adverse events in
1126 gastrointestinal cancers: A pooled analysis of clinical trial and real-world data. Journal of
1127 Clinical Oncology *42*, 169-169. 10.1200/JCO.2024.42.3_suppl.169.

1128 32. Reed, S.C., Croessmann, S., and Park, B.H. (2023). CHIP Happens: Clonal Hematopoiesis of
1129 Indeterminate Potential and Its Relationship to Solid Tumors. Clin Cancer Res *29*, 1403-
1130 1411. 10.1158/1078-0432.Ccr-22-2598.

1131 33. Rondeau, V., Bansal, S., Buttigieg, M.M., Zeng, A.G.X., Chan, D.Y., Chan-Seng-Yue, M., Jin,
1132 L., McLeod, J., Kates, M., Donato, E., et al. (2026). Response to Immune Checkpoint
1133 Blockade Is Enhanced in the Presence of Hematopoietic TET2 Inactivation. Cancer
1134 Research, OF845-OF857. 10.1158/0008-5472.CAN-24-3329.

1135 34. Nguyen, B., Fong, C., Luthra, A., Smith, S.A., DiNatale, R.G., Nandakumar, S., Walch, H.,
1136 Chatila, W.K., Madupuri, R., Kundra, R., et al. (2022). Genomic characterization of
1137 metastatic patterns from prospective clinical sequencing of 25,000 patients. Cell *185*, 563-
1138 575.e511. https://doi.org/10.1016/j.cell.2022.01.003.

1139 35. Quivoron, C., Couronne, L., Della Valle, V., Lopez, C.K., Plo, I., Wagner-Ballon, O., Do
1140 Cruzeiro, M., Delhommeau, F., Arnulf, B., Stern, M.H., et al. (2011). TET2 inactivation
1141 results in pleiotropic hematopoietic abnormalities in mouse and is a recurrent event
1142 during human lymphomagenesis. Cancer Cell *20*, 25-38. S1535-6108(11)00225-X [pii]

1143 10.1016/j.ccr.2011.06.003.

1144 36. Stadtfeld, M., and Graf, T. (2005). Assessing the role of hematopoietic plasticity for
1145 endothelial and hepatocyte development by non-invasive lineage tracing. Development
1146 *132*, 203-213. 10.1242/dev.01558.

1147 37. Lee, P.P., Fitzpatrick, D.R., Beard, C., Jessup, H.K., Lehar, S., Makar, K.W., Pérez-Melgosa,
1148 M., Sweetser, M.T., Schlissel, M.S., Nguyen, S., et al. (2001). A critical role for Dnmt1 and
1149 DNA methylation in T cell development, function, and survival. Immunity *15*, 763-774.
1150 10.1016/s1074-7613(01)00227-8.

1151 38. Rickert, R.C., Roes, J., and Rajewsky, K. (1997). B lymphocyte-specific, Cre-mediated
1152 mutagenesis in mice. Nucleic Acids Res *25*, 1317-1318. 10.1093/nar/25.6.1317.

1153 39. Clausen, B.E., Burkhardt, C., Reith, W., Renkawitz, R., and Forster, I. (1999). Conditional
1154 gene targeting in macrophages and granulocytes using LysMcre mice. Transgenic Res *8*,
1155 265-277. 10.1023/a:1008942828960.

1156 40. Nakayama, M., Hong, C.P., Oshima, H., Sakai, E., Kim, S.-J., and Oshima, M. (2020). Loss of
1157 wild-type p53 promotes mutant p53-driven metastasis through acquisition of survival and
1158 tumor-initiating properties. Nature Communications *11*, 2333. 10.1038/s41467-020-
1159 16245-1.

1160 41. Huang, D.W., Sherman, B.T., Tan, Q., Collins, J.R., Alvord, W.G., Roayaei, J., Stephens, R.,
1161 Baseler, M.W., Lane, H.C., and Lempicki, R.A. (2007). The DAVID Gene Functional
1162 Classification Tool: a novel biological module-centric algorithm to functionally analyze
1163 large gene lists. Genome Biology *8*, R183. 10.1186/gb-2007-8-9-r183.

1164 42. Subramanian, A., Tamayo, P., Mootha, V.K., Mukherjee, S., Ebert, B.L., Gillette, M.A.,
1165 Paulovich, A., Pomeroy, S.L., Golub, T.R., Lander, E.S., and Mesirov, J.P. (2005). Gene set
1166 enrichment analysis: a knowledge-based approach for interpreting genome-wide
1167 expression profiles. Proc Natl Acad Sci U S A *102*, 15545-15550. 0506580102 [pii]

1168 10.1073/pnas.0506580102.

1169 43. Godec, J., Tan, Y., Liberzon, A., Tamayo, P., Bhattacharya, S., Butte, A.J., Mesirov, J.P., and
1170 Haining, W.N. (2016). Compendium of Immune Signatures Identifies Conserved and
1171 Species-Specific Biology in Response to Inflammation. Immunity *44*, 194-206.
1172 10.1016/j.immuni.2015.12.006.

1173 44. Aibar, S., González-Blas, C.B., Moerman, T., Huynh-Thu, V.A., Imrichova, H., Hulselmans,
1174 G., Rambow, F., Marine, J.-C., Geurts, P., Aerts, J., et al. (2017). SCENIC: single-cell
1175 regulatory network inference and clustering. Nature Methods *14*, 1083-1086.
1176 10.1038/nmeth.4463.

1177 45. Zhang, C., Sheng, Q., Zhang, X., Xu, K., Jin, X., Zhou, W., Zhang, M., Lv, D., Yang, C., Li, Y., et
1178 al. (2023). Prioritizing exhausted T cell marker genes highlights immune subtypes in pan-
1179 cancer. iScience *26*, 106484. https://doi.org/10.1016/j.isci.2023.106484.

1180 46. Trapnell, C., Cacchiarelli, D., Grimsby, J., Pokharel, P., Li, S., Morse, M., Lennon, N.J., Livak,
1181 K.J., Mikkelsen, T.S., and Rinn, J.L. (2014). The dynamics and regulators of cell fate

1182 decisions are revealed by pseudotemporal ordering of single cells. Nature Biotechnology
1183 *32*, 381-386. 10.1038/nbt.2859.

1184 47. Borcherding, N., Bormann, N.L., and Kraus, G. (2020). scRepertoire: An R-based toolkit for
1185 single-cell immune receptor analysis. F1000Res *9*, 47. 10.12688/f1000research.22139.2.

1186 48. Bosco, N., Swee, L.K., Bénard, A., Ceredig, R., and Rolink, A. (2010). Auto-reconstitution of
1187 the T-cell compartment by radioresistant hematopoietic cells following lethal irradiation
1188 and bone marrow transplantation. Experimental Hematology *38*, 222-232.e222.
1189 https://doi.org/10.1016/j.exphem.2009.12.006.

1190 49. Busque, L., Patel, J.P., Figueroa, M.E., Vasanthakumar, A., Provost, S., Hamilou, Z., Mollica,
1191 L., Li, J., Viale, A., Heguy, A., et al. (2012). Recurrent somatic TET2 mutations in normal
1192 elderly individuals with clonal hematopoiesis. Nature Genetics *44*, 1179-1181.
1193 10.1038/ng.2413.

1194 50. Zehir, A., Benayed, R., Shah, R.H., Syed, A., Middha, S., Kim, H.R., Srinivasan, P., Gao, J.,
1195 Chakravarty, D., Devlin, S.M., et al. (2017). Mutational landscape of metastatic cancer
1196 revealed from prospective clinical sequencing of 10,000 patients. Nature Medicine *23*,
1197 703-713. 10.1038/nm.4333.

1198 51. Jaiswal, S. (2020). Clonal hematopoiesis and nonhematologic disorders. Blood *136*, 1606-
1199 1614. 10.1182/blood.2019000989.

1200 52. Fraietta, J.A., Nobles, C.L., Sammons, M.A., Lundh, S., Carty, S.A., Reich, T.J., Cogdill, A.P.,
1201 Morrissette, J.J.D., DeNizio, J.E., Reddy, S., et al. (2018). Disruption of TET2 promotes the
1202 therapeutic efficacy of CD19-targeted T cells. Nature *558*, 307-312. 10.1038/s41586-018-
1203 0178-z.

1204 53. Dimitri, A.J., Baxter, A.E., Chen, G.M., Hopkins, C.R., Rouin, G.T., Huang, H., Kong, W.,
1205 Holliday, C.H., Wiebking, V., Bartoszek, R., et al. (2024). TET2 regulates early and late
1206 transitions in exhausted CD8(+) T cell differentiation and limits CAR T cell function. Sci Adv
1207 *10*, eadp9371. 10.1126/sciadv.adp9371.

1208 54. Wang, Y., Sano, S., Yura, Y., Ke, Z., Sano, M., Oshima, K., Ogawa, H., Horitani, K., Min, K.D.,
1209 Miura-Yura, E., et al. (2020). Tet2-mediated clonal hematopoiesis in nonconditioned mice
1210 accelerates age-associated cardiac dysfunction. JCI Insight *5*. 10.1172/jci.insight.135204.

1211 55. Fuster, J.J., MacLauchlan, S., Zuriaga, M.A., Polackal, M.N., Ostriker, A.C., Chakraborty, R.,
1212 Wu, C.L., Sano, S., Muralidharan, S., Rius, C., et al. (2017). Clonal hematopoiesis associated
1213 with TET2 deficiency accelerates atherosclerosis development in mice. Science *355*, 842-
1214 847. 10.1126/science.aag1381.

1215 56. Jaiswal, S., Natarajan, P., Silver Alexander, J., Gibson Christopher, J., Bick Alexander, G.,
1216 Shvartz, E., McConkey, M., Gupta, N., Gabriel, S., Ardissino, D., et al. Clonal Hematopoiesis
1217 and Risk of Atherosclerotic Cardiovascular Disease. New England Journal of Medicine *377*,
1218 111-121. 10.1056/NEJMoa1701719.

1219 57. Sano, S., Oshima, K., Wang, Y., MacLauchlan, S., Katanasaka, Y., Sano, M., Zuriaga, M.A.,
1220 Yoshiyama, M., Goukassian, D., Cooper, M.A., et al. (2018). Tet2-Mediated Clonal

1221 Hematopoiesis Accelerates Heart Failure Through a Mechanism Involving the IL-
1222 1β/NLRP3 Inflammasome. J Am Coll Cardiol *71*, 875-886. 10.1016/j.jacc.2017.12.037.

1223 58. Bolton, K.L., Gillis, N.K., Coombs, C.C., Takahashi, K., Zehir, A., Bejar, R., Garcia-Manero, G.,
1224 Futreal, A., Jensen, B.C., Diaz, L.A., Jr., et al. (2019). Managing Clonal Hematopoiesis in
1225 Patients With Solid Tumors. J Clin Oncol *37*, 7-11. 10.1200/jco.18.00331.

1226 59. Li, S., Feng, J., Wu, F., Cai, J., Zhang, X., Wang, H., Fetahu, I.S., Iwanicki, I., Ma, D., Hu, T., et
1227 al. (2020). TET2 promotes anti-tumor immunity by governing G-MDSCs and CD8+ T-cell
1228 numbers. EMBO reports *21*, e49425. https://doi.org/10.15252/embr.201949425.

1229 60. Carty, S.A., Gohil, M., Banks, L.B., Cotton, R.M., Johnson, M.E., Stelekati, E., Wells, A.D.,
1230 Wherry, E.J., Koretzky, G.A., and Jordan, M.S. (2018). The Loss of TET2 Promotes CD8(+) T
1231 Cell Memory Differentiation. J Immunol *200*, 82-91. 10.4049/jimmunol.1700559.

1232 61. Yue, X., Trifari, S., Äijö, T., Tsagaratou, A., Pastor, W.A., Zepeda-Martínez, J.A., Lio, C.W., Li,
1233 X., Huang, Y., Vijayanand, P., et al. (2016). Control of Foxp3 stability through modulation of
1234 TET activity. J Exp Med *213*, 377-397. 10.1084/jem.20151438.

1235 62. Khan, O., Giles, J.R., McDonald, S., Manne, S., Ngiow, S.F., Patel, K.P., Werner, M.T., Huang,
1236 A.C., Alexander, K.A., Wu, J.E., et al. (2019). TOX transcriptionally and epigenetically
1237 programs CD8+ T cell exhaustion. Nature *571*, 211-218. 10.1038/s41586-019-1325-x.

1238 63. Kim, K., Park, S., Park, S.Y., Kim, G., Park, S.M., Cho, J.W., Kim, D.H., Park, Y.M., Koh, Y.W.,
1239 Kim, H.R., et al. (2020). Single-cell transcriptome analysis reveals TOX as a promoting
1240 factor for T cell exhaustion and a predictor for anti-PD-1 responses in human cancer.
1241 Genome Med *12*, 22. 10.1186/s13073-020-00722-9.

1242 64. Zhang, X., Wang, Y., Xue, H., Zhao, Y., Liu, M., Wei, H., and Liu, Q. (2025). Clonal
1243 hematopoiesis of indeterminate potential and risk of autoimmune thyroid disease. BMC
1244 Med *23*, 237. 10.1186/s12916-025-04077-z.

1245 65. Liu, Q., Wästerlid, T., Smedby, K.E., Xue, H., Boberg, E., Fang, F., and Liu, X. (2025). Clonal
1246 hematopoiesis of indeterminate potential and risk of immune thrombocytopenia. J Intern
1247 Med *297*, 672-682. 10.1111/joim.20092.

1248 66. Jaber Chehayeb, R., Singh, J., Matute-Martinez, C., Chen, N.W., Guajardo, A.F., Lin, D.,
1249 Jayakrishnan, R., Christofides, A., Leveille, E., Im, Y., et al. (2024). Clonal hematopoiesis of
1250 indeterminate potential is associated with increased risk of immune checkpoint inhibitor
1251 myocarditis in a prospective study of a cardio-oncology cohort. Cardiooncology *10*, 84.
1252 10.1186/s40959-024-00289-z.

1253 67. Gao, Q., Shen, K., and Xiao, M. (2024). TET2 mutation in acute myeloid leukemia: biology,
1254 clinical significance, and therapeutic insights. Clin Epigenetics *16*, 155. 10.1186/s13148-
1255 024-01771-2.

1256 68. An, J., González-Avalos, E., Chawla, A., Jeong, M., López-Moyado, I.F., Li, W., Goodell, M.A.,
1257 Chavez, L., Ko, M., and Rao, A. (2015). Acute loss of TET function results in aggressive
1258 myeloid cancer in mice. Nature Communications *6*, 10071. 10.1038/ncomms10071.

1259 69. Muto, H., Sakata-Yanagimoto, M., Nagae, G., Shiozawa, Y., Miyake, Y., Yoshida, K., Enami,
1260 T., Kamada, Y., Kato, T., Uchida, K., et al. (2014). Reduced TET2 function leads to T-cell

1261 lymphoma with follicular helper T-cell-like features in mice. Blood Cancer J *4*, e264.
1262 10.1038/bcj.2014.83.

1263 70. Vanner, R., Zeng, A.G.X., Chan-Seng-Yue, M., Bansal, S., Donato, E., Jin, L., Genta, S., Sanz
1264 Garcia, E., Chan, S.M., Trumpp, A., and Dick, J.E. (2023). Somatic TET2 Mutations Prime the
1265 Immune System for Response to Immune Checkpoint Blockade. Blood *142*, 2689-2689.
1266 10.1182/blood-2023-177740.

1267 71. Carty, S.A., Gohil, M., Koretzky, G.A., and Jordan, M.S. (2014). TET2 Regulates CD8+ T Cell
1268 Differentiation. Blood *124*, 1423-1423. 10.1182/blood.V124.21.1423.1423.

1269 72. Sakai, E., Nakayama, M., Oshima, H., Kouyama, Y., Niida, A., Fujii, S., Ochiai, A., Nakayama,
1270 K.I., Mimori, K., Suzuki, Y., et al. (2018). Combined Mutation of Apc, Kras, and Tgfbr2
1271 Effectively Drives Metastasis of Intestinal Cancer. Cancer Research *78*, 1334-1346.
1272 10.1158/0008-5472.CAN-17-3303.

1273 73. Fujisawa, M., Nguyen, T.B., Abe, Y., Suehara, Y., Fukumoto, K., Suma, S., Makishima, K.,
1274 Kaneko, C., Nguyen, Y.T.M., Usuki, K., et al. (2022). Clonal germinal center B cells function
1275 as a niche for T-cell lymphoma. Blood *140*, 1937-1950. 10.1182/blood.2022015451.

1276 74. Krämer, A., Green, J., Pollard, J., Jr., and Tugendreich, S. (2014). Causal analysis approaches
1277 in Ingenuity Pathway Analysis. Bioinformatics *30*, 523-530. 10.1093/bioinformatics/btt703.

1278 75. Hao, Y., Stuart, T., Kowalski, M.H., Choudhary, S., Hoffman, P., Hartman, A., Srivastava, A.,
1279 Molla, G., Madad, S., Fernandez-Granda, C., and Satija, R. (2024). Dictionary learning for
1280 integrative, multimodal and scalable single-cell analysis. Nature Biotechnology *42*, 293-
1281 304. 10.1038/s41587-023-01767-y.

1282 76. Germain, P.L., Lun, A., Garcia Meixide, C., Macnair, W., and Robinson, M.D. (2021).
1283 Doublet identification in single-cell sequencing data using scDblFinder. F1000Res *10*, 979.
1284 10.12688/f1000research.73600.2.

1285 77. Venturi, V., Kedzierska, K., Turner, S.J., Doherty, P.C., and Davenport, M.P. (2007).
1286 Methods for comparing the diversity of samples of the T cell receptor repertoire. J
1287 Immunol Methods *321*, 182-195. 10.1016/j.jim.2007.01.019.

1288 78. Thomas, P.G., Handel, A., Doherty, P.C., and La Gruta, N.L. (2013). Ecological analysis of
1289 antigen-specific CTL repertoires defines the relationship between naïve and immune T-cell
1290 populations. Proceedings of the National Academy of Sciences *110*, 1839-1844.
1291 10.1073/pnas.1222149110.

1292 79. Greiff, V., Bhat, P., Cook, S.C., Menzel, U., Kang, W., and Reddy, S.T. (2015). A
1293 bioinformatic framework for immune repertoire diversity profiling enables detection of
1294 immunological status. Genome Medicine *7*, 49. 10.1186/s13073-015-0169-8.

1295 80. Miura, F., Shibata, Y., Miura, M., Sangatsuda, Y., Hisano, O., Araki, H., and Ito, T. (2019).
1296 Highly efficient single-stranded DNA ligation technique improves low-input whole-genome
1297 bisulfite sequencing by post-bisulfite adaptor tagging. Nucleic Acids Research *47*, e85-e85.
1298 10.1093/nar/gkz435.

1299 81. Miura, F., Shibata, Y., Miura, M., Inatomi, K., Suzuki, Y., and Ito, T. (2025). Identification of
1300 an enzyme with strong single-stranded DNA ligation activity and its application for
1301 sequencing. Nucleic Acids Research *53*, gkaf054. 10.1093/nar/gkaf054.

1302 82. Krueger, F., and Andrews, S.R. (2011). Bismark: a flexible aligner and methylation caller for
1303 Bisulfite-Seq applications. Bioinformatics *27*, 1571-1572. 10.1093/bioinformatics/btr167.

1304